Assessment of low-fidelity fluid–structure interaction model for flexible propeller blades

Sodja, Jurij; De Breuker, Roeland; Nozak, Dejan; Drazumeric, Radovan; Marzocca, Pier

DOI
10.1016/j.ast.2018.03.044

Publication date
2018

Document Version
Accepted author manuscript

Published in
Aerospace Science and Technology

Citation (APA)
Sodja, J., De Breuker, R., Nozak, D., Drazumeric, R., & Marzocca, P. (2018). Assessment of low-fidelity fluid–structure interaction model for flexible propeller blades. *Aerospace Science and Technology*, *78*, 71-88. https://doi.org/10.1016/j.ast.2018.03.044

Assessment of Low-Fidelity Fluid-Structure Interaction Model for Flexible Propeller Blades

Jurij Sodja[1], Roeland De Breuker[2]
Delft University of Technology, The Netherlands,

Dejan Nozak[3], Radovan Drazumeric[4]
University of Ljubljana, Slovenia

and

Pier Marzocca[5]
RMIT University, Australia

Abstract

Low-fidelity fluid-structure interaction model of flexible propeller blades is assessed by means of comparison with high-fidelity aeroelastic results. The low-fidelity model is based on a coupled extended blade-element momentum model and non-linear beam theory which were both implemented in Matlab. High-fidelity fluid-structure interaction analysis is based on coupling commercial computational fluid dynamics and computational structural dynamics codes. For this purpose, Ansys CFX® and Ansys Mechanical® were used. Three different flexible propeller blade geometries are considered in this study: straight, backward swept, and forward swept. The specific backward and forward swept blades are chosen due to their aeroelastic response and its influence on the propulsive performance of the blade while a straight blade was selected in order to serve as a reference. First, the high-fidelity method is validated against experimental data available for the selected blade geometries. Then the high- and low-fidelity methods are compared in terms of integral thrust and breaking power as well as their respective distributions along the blades are compared for different advancing ratios. In a structural sense, the comparison is performed by analysing the blade bending and

[1] Research Associate, Aerospace Structures and Materials, Faculty of Aerospace Engineering, Kluyverweg 1, 2629 HS Delft, The Netherlands; J.Sodja@tudelft.nl.
[2] Associate Professor, Aerospace Structures and Materials, Faculty of Aerospace Engineering, Kluyverweg 1, 2629 HS Delft, The Netherlands.
[3] Teaching Assistant, Laboratory for Aeronautics, Faculty of Mechanical Engineering, Askerceva 6, SI-1000 Ljubljana, Slovenia.
[4] Research Associate, Faculty of Mechanical Engineering, Askerceva 6, SI-1000 Ljubljana, Slovenia.
[5] Professor and Associate Dean of Engineering, Aerospace Engineering and Aviation, PO Box 71 Bundoora VIC 3083, Australia.

DOI: https://doi.org/10.1016/j.ast.2018.03.044

torsional deformation. Based on the obtained results, given the simplicity of the low-fidelity method, it can be concluded that the agreement between the two methods is reasonably good. Moreover, an important result of the comparison study is an observation that the advance ratio is no longer a valid measure of similarity in the case of flexible propeller blades and the behaviour of such blades can change significantly with changing operating conditions while keeping the advance ratio constant. This observation is supported by both high- and low-fidelity methods.

Nomenclature

Variables:

a_z	axial interference factor
a_φ	rotational interference factor
c	blade element chord length
C_L	airfoil lift coefficient
C_P	power coefficient, $P/\rho n^3 D^5$
C_T	thrust coefficient, $T/\rho n^2 D^4$
C_Z	axial force coefficient
C_φ	torque coefficient
D	propeller diameter
E	tensile modulus
$\vec{e}_D$	unit vector in direction of drag on the blade element
$\vec{e}_L$	unit vector in direction of lift on the blade element
$\vec{e}_r, \vec{e}_\varphi, \vec{e}_z$	polar coordinate system
$\vec{e}_x, \vec{e}_y, \vec{e}_z$	global coordinate system
$\vec{e}_\xi, \vec{e}_\eta, \vec{e}_\zeta$	local mechanical coordinate system
F	Prandtl's momentum loss factor
G	shear modulus
$\bar{I}_t$	non-dimensional cross-sectional torsion constant
$\bar{I}_\eta, \bar{I}_\zeta$	non-dimensional cross-sectional moments of inertia along $\vec{e}_\eta$ and $\vec{e}_\zeta$
J	advance ratio, v_0/nD
M_ξ, M_η, M_ζ	moments along axis of local mechanical coordinate system
$M_{\xi 0}$, $M_{\eta 0}$, $M_{\zeta 0}$	Initial moments along axis of local mechanical coordinate system
n	revolutions per second
N_B	number of propeller blades
P	braking power
r, φ, z	coordinates along basis vectors $\vec{e}_r$, $\vec{e}_\varphi$, $\vec{e}_z$
R_H	hub radius
R_T	tip radius
s	arc length
T	thrust
v^*	velocity in the plane of the blade element
v_0	advance velocity

x, y, z	coordinates along basis vectors $\vec{e}_x$, $\vec{e}_y$, $\vec{e}_z$
z_0	blade axis tip coordinate along $\vec{e}_z$
β	blade pitch angle
β_0	initial blade pitch angle
β_{75}	blade pitch at $0.75\ R_T$
$\Delta\beta$	blade torsional deformation
$\Delta y, \Delta z$	blade deflection along $\vec{e}_y$, and $\vec{e}_z$
ε	drag-to-lift ratio, C_D/C_L
η	propeller efficiency
μ	dynamic viscosity
ρ	air density
ρ_b	material density comprising the blade
$\rho_{\eta 0}, \rho_{\zeta 0}$	initial blade axis curvature in the direction of $\vec{e}_\eta$ and $\vec{e}_\zeta$
ϕ	blade axis parameter
φ_0	blade axis tip coordinate along $\vec{e}_\varphi$
χ	non-dimensional radius, r/R_T
ω	propeller angular velocity

Acronyms:

ALE-VMS	arbitrary Lagrangian–Eulerian variational multiscale
BB	backward swept blade
BEM	blade-element momentum model
CFD	computational fluid dynamics
CSD	computational structural dynamics
eBEM	extended blade-element momentum model
FB	forward swept blade
FEM	finite element model
FSI	fluid-structure interaction
H-F	high-fidelity
L-F	low-fidelity
RANS/VLM	Reynolds-averaged Navier-Stokes/vortex line method
SB	straight blade

1 Introduction

Performance of propeller blades can be improved over a range of operating conditions by treating the blades as elastic and accounting for their aeroelastic response which can be optimized for a desired objective [1]. In preliminary design stage, such optimization requires many evaluations of various blade configurations at different operating conditions which is a numerically intensive task. A fast, robust, and widely applicable low-fidelity model is therefore required. Low-fidelity model based on a fluid-structure interaction (FSI) model proposed by Sodja et al. [1] is compared against a high-fidelity FSI simulation based on commercially available codes for computational fluid

dynamics (CFD) and computational structural dynamics (CSD). The purpose of the comparison is to provide better insight into the modelling capabilities of the proposed low-fidelity model which is critical for understanding its applicability limitations and for the interpretation of the low-fidelity results. Moreover, even though advancements in high-performance computing and advanced numerical methods make it possible to simulate complex fluid-structure interaction problems such as the structural response of flexible propeller or wind turbine blades to aerodynamic and inertial loads, the overall computational costs are still too high to employ these methods in practical design process. In order to reduce the computational costs several multi- and variable-fidelity methods have been proposed in the past, for instance by Kwon et al.[2] , Piancastelli et al.[3] and Nigam et al.[4], which rely on low-fidelity methods such as the one proposed by Sodja et al.[1].

Even though computers have experienced an extraordinary headway in terms of their computational power, fully coupled high-fidelity FSI simulations of rotary wing applications are still scarce. Among others, Tojo and Marta [5], Bazilevs et al. [6] have successfully applied a fully coupled CFD-CSD analysis to the entire rotor of a wind turbine. Due to computational intensity and lengthy nature of fully coupled FSI simulations many authors still resort to either one-way high-fidelity FSI simulations, mixed-fidelity CFD-CSD or low-fidelity CFD combined with high-fidelity CSD methods. Bazilevs et al. [7] developed a computational procedure for one-way FSI simulations for pre-bending of wind turbine blades. Firstly, flow characteristics were computed on the deformed shape of the blade at the specified design point. The resulting aerodynamic loads were then applied to the structural model in order to calculate the undeformed stress-free geometry of the blade. An example of mixed-fidelity CFD-CSD method was proposed by Braaten et al. [8] who applied a two-way coupled Reynolds-Averaged Navier-Stokes/Vortex Line Method (RANS/VLM) with composite shell finite element model (FEM). Both steady state and transient performance analysis of the rotor design were performed. As reported by the authors, the employment of the RANS/VLM CFD method allowed a reasonably small CFD mesh, to perform efficient transient simulations in reasonable times. Hsu and Bazilevs [9] coupled a low-order FEM arbitrary Lagrangian–Eulerian variational multiscale (ALE-VMS) CFD method with thin composite shell isogeometric analysis and applied it to the entire wind turbine rotor along with its nacelle and supporting tower. The proposed approach is claimed to yield a balanced combination of efficiency, accuracy and flexibility.

This paper contributes to the state of the art in two way: a) by providing a detailed assessment of the proposed low-fidelity aeroelastic propeller model and b) by investigating the deficiency of the advance ratio as a similarity criterion in the case of flexible propeller blades.

A detailed assessment of the proposed low-fidelity aeroelastic propeller model is facilitated by comparing to the results obtained using commercially available CFD and CSD methods. The assessment is based on comparing the aeroelastic performance of three different blades each exhibiting fundamentally different aeroelastic behavior. Moreover, the aeroelastic capabilities of the low-fidelity model are assessed by comparing integral performance measures such as thrust, breaking power and propulsive efficiency as well as their respective distributions along the blade. Structural deformations along the blades are investigated and compared as well.

The second important contribution deals with the deficiency of the advance ratio as a similarity criterion as far as flexible propeller blades are concerned. The low-fidelity model indicated that for flexible propeller blades the advance ratio can no longer serve as a similarity criterion in terms of aerodynamic performance which was confirmed using the high-fidelity method.

The paper is organized as follows. First, the geometries of the analyzed blades are presented in section 2. The low-fidelity model is briefly discussed in section 3, a more detailed presentation can be found in [1]. A detailed description of the FSI setup is supplied in section 4. A description of computational fluid and structural domains, their sizing and the used meshing technique is given. The initial and boundary conditions pertinent to CFD and CSD codes are also described in this section. Section 5 contains the results of the FSI analyses. CFD results refer to the performance characteristics of the blades, namely the thrust, turning power and efficiency as well as to their respective distributions along the blade. CSD results refer to the bending and torsional deformation of the blades induced by the aerodynamic and inertial loads. Observations and conclusions are summarized in section 6.

2 Blade Geometry

The geometry of the simulated blades was selected based on the influence of their shape, namely, of their respective blade axis, on their aerodynamic performance. An interested reader can consult the paper written by Sodja et al. [1] for more information on how the overall geometry of the blades was derived. It was established there that the aerodynamic response of a flexible propeller blade to changing operating conditions strongly depends on the shape of the blade's elastic axis. It was found that the blades swept backward (BB) and the blades swept forward (FB) exhibited

an improved and reduced performance with respect to the straight blade (SB), which served as a reference geometry. It is noteworthy that the BB and the FB blades were optimized with an objective to emphasize the afore mentioned effects. Therefore, these three blade geometries were selected for the comparison of the low- and high-fidelity FSI analysis since it is expected that the difference in the results should be most noticeable.

The blade axis geometry is expressed by the Eq. (1) in polar coordinates [1]:

$$\varphi(r) = \frac{\varphi_0}{2}\left(3\left(\frac{r-R_H}{R_T-R_H}\right)^2 - \left(\frac{r-R_H}{R_T-R_H}\right)^3\right),$$
$$z(r) = \frac{z_0}{2}\left(3\left(\frac{r-R_H}{R_T-R_H}\right)^2 - \left(\frac{r-R_H}{R_T-R_H}\right)^3\right), \quad (1)$$

where φ_0 and z_0 represent angular and axial coordinate of the blade tip. While the root of the blade axis is assumed to be at $(R_H, 0, 0)$. The blade axis parameters for the selected blade geometries are listed in Table 1.

Table 1: Selected blade axis parameters

Blade	R_H [m]	R_T [m]	φ_0 [°]	z_0[m]
SB	0.03	0.23	7.7	−0.016
BB	0.03	0.23	−16.5	−0.033
FB	0.03	0.23	12	0.051

The airfoil used in all three blades was Clark-Y. The resulting blade axes are depicted in Fig. 1. The chord length and the pitch angle distributions along the blade axis are presented in Fig. 2, while the final shapes of the blades including the hub design are presented in Fig. 3. It is important to notice that all the blade geometries are given in their undeformed shape. Therefore, even the SB blade, the reference blade, is not completely straight.

Apart from the blade sweep, there are two differences between the SB, BB and FB blade designs noticeable from Fig. 2. Firstly, the chord lengths over the outboard part of the BB and FB blade are longer in comparison to the SB blade. Secondly, the BB blade has less washout towards the tip of the blade in comparison to the SB and FB blade, as can be seen from Fig. 2b. Interestingly, in this case the SB and FB blades have almost identical pitch angle distribution. One has to keep in mind that all the blades were designed to consume the same amount of power at the given design operating conditions. Therefore, due to larger blade sweep, the BB and the FB blade have longer chord lengths in the outboard section of the blade. The difference in the pitch angle is explained, as will be shown later, by the geometric

bend-twist coupling induced by the sweep of each blade. The SB and the FB blades are swept forward in their undeformed shape and hence wash in as the aerodynamic loads are increased. The BB blade is swept backward and hence washes out upon increase of aerodynamic loads.

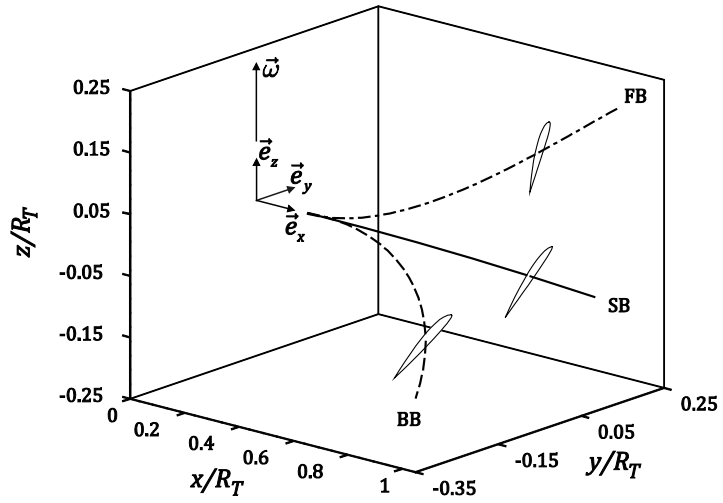

Figure 1: Orientation of the selected blade axes in space

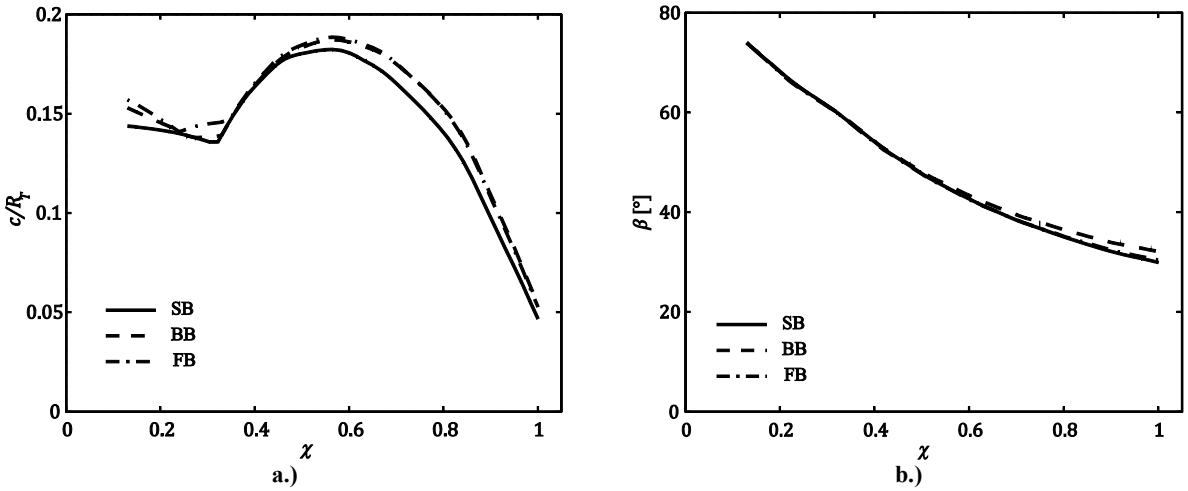

Figure 2. a.) Chord length and b.) pitch angle distribution along the blade

3 Low-Fidelity Fluid-Structure Interaction Model

The low-fidelity FSI model was based on an iteratively coupled extended blade-element momentum model (BEM) and non-linear beam model, which was intended for the design of the flexible propeller blades. However, the model's fidelity in capturing the key phenomena accurately is crucial if the design process is going to yield quality and useful design parameters. Since the derivation of the coupled model was presented in detail in [1], only the key concepts of the FSI model are summarized here for the sake of completeness.

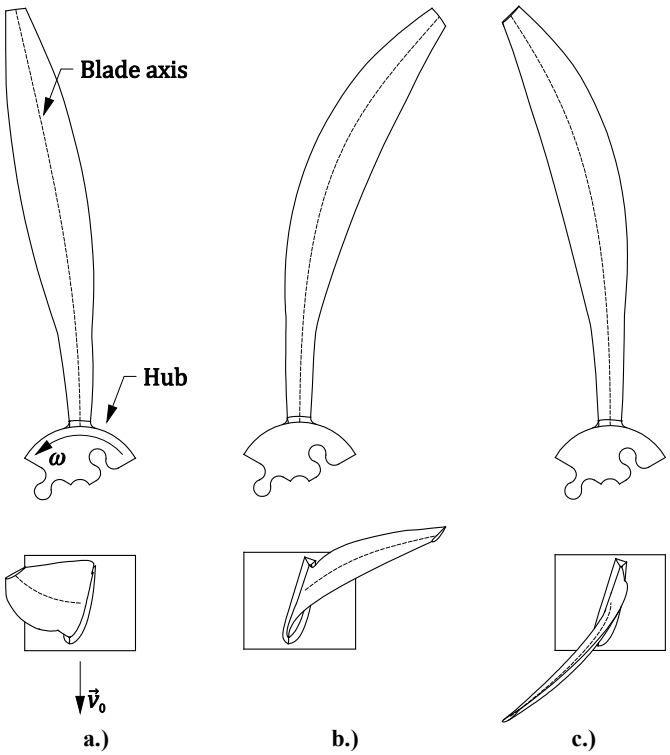

Figure 3. Analyzed blade geometries: a.) SB, b.) BB, and c.) FB

3.1 Extended Blade-Element Momentum Model

The extended blade-element momentum model (eBEM) was developed with the intention of applying the blade-element momentum theory to the blades of arbitrary geometry. Therefore, the original BEM equations had to be modified. For ease of understanding the most important quantities and unit vectors pertaining to the eBEM are shown in Fig. 4.

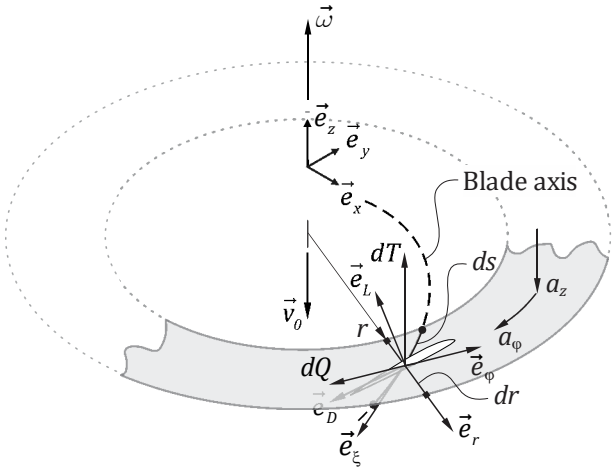

Figure 4: Blade element and disk annulus pertinent to the eBEM model

The blade-element part in terms of thrust, dT/ds, and torque distribution, dQ/ds, was modelled by the following equations [1]:

$$\frac{dT}{ds} = \frac{1}{2}\rho v^{*2} N_B c C_Z, \tag{2}$$

$$\frac{dQ}{ds} = \frac{1}{2}\rho v^{*2} N_B c C_\varphi, \tag{3}$$

where the ρ, v^*, c and N_B present the air density, the airstream velocity in the plane of the cross-section, the airfoil chord and the number of propeller blades. The axial force and shaft torque coefficients, C_Z and C_φ, are expressed as a projection of aerodynamic force along the axial and circumferential direction, $\vec{e}_z$ and $\vec{e}_\varphi$ respectively:

$$C_Z = C_L(\vec{e}_L - \varepsilon\vec{e}_D)\vec{e}_z, \tag{4}$$

$$C_\varphi = C_L(-\vec{e}_L + \varepsilon\vec{e}_D)\vec{e}_\varphi, \tag{5}$$

where C_L and ε present sectional lift coefficient and drag-to-lift ratio. $\vec{e}_L$ and $\vec{e}_D$ are unit vectors in the direction of lift and drag. The momentum part of the model was implemented following Eq. (6) and (7) which express thrust and torque distribution, dT/dr and dQ/dr, in terms of momentum increase of the air passing through an annulus of radius r:

$$\frac{dT}{dr} = 2\pi r\rho v_0(1 + a_z)2v_0 a_z F, \tag{6}$$

$$\frac{dQ}{dr} = 2\pi r\rho v_0(1 + a_z)2\omega r a_\varphi F, \tag{7}$$

where v_0 and ω present propeller's advance and angular velocity. Finite number of the blades comprising the propeller is accounted for by the Prandtl's momentum loss factor, F, which is shown in Eq. (10) for the sake of completeness. The axial and rotational interference factors are calculated following Eqs. (8) and (9):

$$a_z = \frac{N_B c C_z \vec{e}_r \vec{e}_\xi}{8\pi r F\left(\vec{e}_L \vec{e}_\varphi\right)^2 - N_B c C_z \vec{e}_r \vec{e}_\xi}, \tag{8}$$

$$a_\varphi = \frac{N_B c C_\varphi \vec{e}_r \vec{e}_\xi}{-8\pi r F(\vec{e}_L \vec{e}_\varphi)(\vec{e}_L \vec{e}_z) + N_B c C_\varphi \vec{e}_r \vec{e}_\xi}, \tag{9}$$

$$F = \frac{2}{\pi}\arccos(e^{-f}), f = \frac{N_B(1-\chi)\sqrt{1+\chi^2\tan^2\phi}}{2\chi\tan\phi}, \tag{10}$$

where $\vec{e}_r$ and $\vec{e}_\xi$ are radial basis vector in global polar coordinate system and basis vector along the beam axis in local mechanical coordinate system. χ is non-dimensional arc length along the blade.

The fundamental equations (2), (3), (6), and (7) are essentially the same as those proposed by Adkins and Liebeck [10], however, the equations governing the aerodynamic coefficients, C_Z and C_φ, and the interference factors, a_Z and a_φ, were changed in order to bridge correctly the momentum and the blade-element part of the model in the case of a non-straight blade.

3.2 Non-Linear Beam Model

The structural model is based on a geometrically non-linear beam model. The bending is taken into account by Euler-Bernoulli equations, while the torsional deformations are accounted for by applying Saint-Venant theory. Since the analyzed blade geometries are already pre-bent and pre-twisted, the equations governing deformations are formulated as a state equations connecting the initial and the final state of deformation. The governing equations are [1]:

$$\beta' = \beta_0' - \frac{M_\xi - M_{\xi 0}}{c^4 G \bar{I}_t}, \tag{11}$$

$$y'' = \left(\frac{1}{\rho_{\eta 0}} + \frac{M_\eta - M_{\eta 0}}{c^4 E \bar{I}_\eta}\right)\vec{e}_\zeta \vec{e}_y + \left(\frac{1}{\rho_{\zeta 0}} - \frac{M_\zeta - M_{\zeta 0}}{c^4 E \bar{I}_\zeta}\right)\vec{e}_\eta \vec{e}_y, \tag{12}$$

$$z'' = \left(\frac{1}{\rho_{\eta 0}} + \frac{M_\eta - M_{\eta 0}}{c^4 E \bar{I}_\eta}\right)\vec{e}_\zeta \vec{e}_z + \left(\frac{1}{\rho_{\zeta 0}} - \frac{M_\zeta - M_{\zeta 0}}{c^4 E \bar{I}_\zeta}\right)\vec{e}_\eta \vec{e}_z, \tag{13}$$

where y, z, and β present the beam axis coordinates in the global coordinate system, and the blade twist. Unit vectors $\vec{e}_y$, $\vec{e}_z$, and $\vec{e}_\eta$, $\vec{e}_\zeta$ comprise the global and the local mechanical coordinate system, respectively. M_ξ, M_η, M_ζ are instantaneous torsional and bending moments in respective local coordinate directions whereas $M_{\xi 0}$, $M_{\eta 0}$, and $M_{\zeta 0}$ are the moments that correspond to the loads in the initial state of the blades which is described by the initial twist β_0

and the principal curvatures $\rho_{\eta 0}$ and $\rho_{\zeta 0}$. Finally, $c^4 E\bar{I}_\eta$ and $c^4 E\bar{I}_\zeta$ present the cross-sectional bending stiffness in the local mechanical coordinate system with c being the chord, E the tensile modulus, and $\bar{I}_\eta$ and $\bar{I}_\zeta$ the respective non-dimensional cross-sectional moments of inertia.

4 High-Fidelity Fluid-Structure Interaction Model

Individual components comprising the high-fidelity FSI model are described in this section. First the geometry and mesh preparation are explained in section 4.1. Modelling approach and settings used in CFD and CSD simulations are detailed in sections 4.2 and 4.3. Coupling between CFD and CSD solvers is described in section 4.4.

4.1 Geometry and Mesh Preparation

Blade geometries were modelled in Solidworks® and then exported to Ansys Modeler® where the appropriate computational domain for the CFD analysis was added. A blade with surrounding computational domain is shown in Fig. 5. One third of the entire computational domain was modelled in order to reduce the size of the CFD model [2]. Meshing of both the fluid and the solid computational domain was performed within Ansys Workbench®. In order to simplify the meshing process, a tetragonal mesh with triangular prismatic elements in the blade's boundary layer were employed in the fluid domain. CFD mesh quality was ensured by following recommendations given in the CFX modelling guide [11] and by performing a mesh convergence study, which results are presented in section 5.1

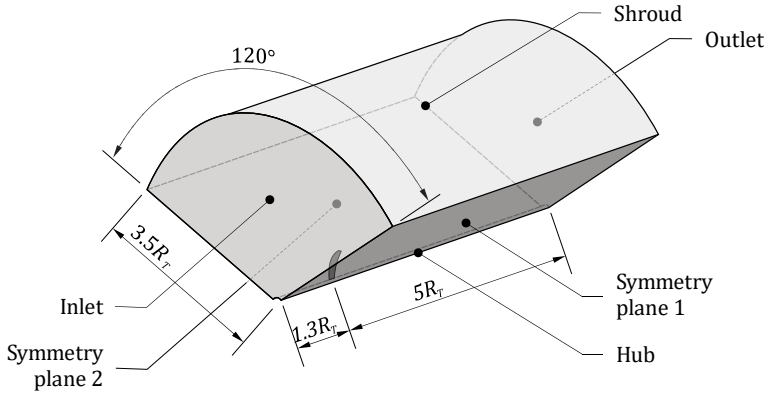

Figure 5. Computational domain

In order to minimize the size and complexity of the structural model the blades were modelled without the hub. Since the hub was a solid block of material it was assumed that it was rigid enough in order to consider the blades rigidly clamped at the root. The solid domain was discretized entirely by triangular prismatic elements oriented along

the blade axis. Meshing was performed in Ansys Workbench. The final discretization of the fluid domain in the proximity of the blade tip is illustrated in Fig. 6.

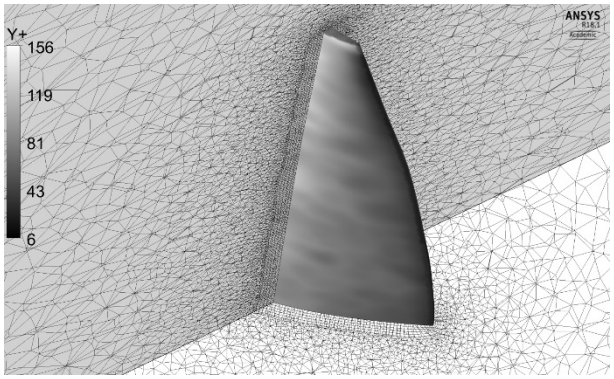

Figure 6. Mesh cross-section at the blade tip and y^+ value on the blade surface

4.2 CFD Simulation Settings

CFD simulations were performed in the Ansys CFX® software. The fluid domain was modelled as incompressible air of density $\rho = 1.2210\ \mathrm{kg/m^3}$ and dynamic viscosity $\mu = 1.98 \cdot 10^{-5}\ \mathrm{kg/ms}$. The simulations were configured as stationary. Turbulence was modelled using standard $k-\varepsilon$ turbulence model along with adaptive wall functions in the boundary layer region. The $k-\varepsilon$ model was selected since it is reported to be a robust model with a good trade-off between turbulence modelling capabilities and numerical efficiency [12]–[14]. Adaptive wall functions enable boundary layer resolution in the wall regions where y^+ value is less than two and boundary flow modelling via scale functions elsewhere. However, later, the analysis of the y^+distribution across the blade revealed that over most of the blade the y^+ assumed values between 5 and 150.

Rotation of the blade was modelled by placing the entire fluid computational domain into a rotating reference frame. The rotating reference frame was set to rotate with a constant angular velocity of $315\ \mathrm{rad/s}$.

Boundary conditions were specified on the relevant geometric surfaces as indicated in Fig. 5 in the following manner. At the inlet boundary inflow turbulence intensity of 5% and a normal velocity in the stationary reference frame were prescribed therewith simulating the propeller advancing velocity. A type opening boundary condition with a relative pressure of 0 Pa was prescribed at the outlet and shroud boundary. The opening boundary condition allows the fluid to enter or exit the computational domain. The hub extended throughout the entire length of the computational domain. In order to avoid introducing unwanted vorticity into the flow the hub was modelled as a slip-free wall. Axial symmetry of the problem was exploited in order to reduce the size of the computational domain [13]–[17]. Therefore,

the periodic boundary condition was assigned to the two symmetry planes. A rotating no-slip wall boundary condition was assigned on the blade surface. Furthermore, an FSI interface was assigned to the blade surface in order to communicate the aerodynamic loads and displacements between CFD and CSD solver.

4.3 CSD Simulation Settings

The blade was modelled using an isotropic material having the same material properties used in the low-fidelity model. The finite element used was a SOLID186, which belongs to a group of a higher-order finite elements exhibiting quadratic displacement behavior. SOLID186 finite elements are well suited for modelling irregular shapes enclosed by curved boundaries. The elements were used in the form of "Homogenous Structural Solid" with integration scheme set to full. Full integration scheme was selected due to a small number of elements in the thickness direction of the airfoil [18].

Specified material properties were material density, elastic and shear modulus, ρ_b, E and G, respectively. The values $\rho_b = 1120\ \mathrm{kg/m^3}$, $E = 2.34$ GPa and $G = 900$ MPa were acquired from the resin datasheet that was used in the blade manufacturing process[6].

A fluid-structure interface type of boundary condition was prescribed over the entire "wet" surface of the blade. At the root of the blade, where the blade attached to the hub, a boundary condition of type "fixed support" was set to simulate the clamped boundary condition. Furthermore, rotation of the blade was modelled by specifying rotational velocity to the global coordinate system with its rotating axis aligned along the propeller rotational axis.

4.4 Coupling of Computational Fluid and Structural Dynamics

Blade deformation has a strong influence on the blade aerodynamic performance. Therefore, a two-way coupling among the structural and fluid field solvers is required. In the current case, the ANSYS Mechanical and ANSYS CFX are coupled in a two-way iterative manner as shown in Fig. 7. A solution is obtained by performing stagger iterations between the solid and the fluid field solver within each time step until coupling convergence criteria are met or the maximum number of stagger iterations is exceeded. In every stagger iteration, first, the blade deformation and aerodynamic loads are exchanged between the two solvers. Then each solver is run separately until their pertinent convergence criteria are met or the maximum number of equilibrium loops in the case of ANSYS Mechanical or the

[6] Obtained from resin manufacturer's web site: http://www.dsm.com [retrieved Jun. 2012]

maximum number of coefficient loops in the case of ANSYS CFX is reached. If, at any level of the solution process, the maximum number of iterations is reached then the solver proceeds with the data set obtained in the last iteration. Hence it is up to the user to check whether sufficient convergence is achieved in the end.

Even though high-fidelity simulations were configured as stationery, time stepping was used in order to initialize the FSI model and to vary the simulation parameters. The coupled CFD-CSD model is sensitive to inconsistent initial conditions [19]. Hence, time marching was used to gradually ramp-up the inflow velocity in the CFD solver. Therewith, consistent loads and displacements were obtained across the CFD and CSD solver in the initialization phase of the simulation. Secondly, during the performed parametric studies, the inflow velocity and the propeller rotational velocity were varied. By employing time marching these two parameters could be changed from one time step to another, while the solution from the previous time step was used as an initial guess. This way initialization of the FSI model for every parameter change could be avoided, which led to faster execution of the performed parametric studies.

In the current case, the following convergence criteria and maximum number of solver evaluations were used. The normalized residual for the coupling data exchanged between ANSYS Mechanical and ANSYS CFX was set to $1 \cdot 10^{-4}$ with a maximum of five stagger iterations per time step. The root-mean-square (RMS) normalized residual for the mass and momentum equations in the CFX solver was set to $1 \cdot 10^{-6}$ with the maximum of 15 coefficient loops per stagger iteration. The ANSYS Mechanical convergence target was set to 0.001 fraction of the second norm of the applied load and total displacement. The maximum number of equilibrium iterations was limited to 15. The prescribed maximum number of equilibrium and coefficient loops in ANSYS Mechanical and ANSYS CFX solver controls the convergence of each solver within individual stagger iteration. However, within every stagger iteration each solver does not need to reach final convergence level. Final convergence level only needs to be achieved in the last coupling step. This way the high-fidelity solution can be adequately evolved while keeping a low number of high-fidelity solver evaluations, which considerably speeds up the high-fidelity simulations.

The coupling between the ANSYS CFX and ANSYS Mechanical was realized by ANSYS MFX server, which takes care of transferring and mapping the data between the two field solvers at the beginning of every stagger iteration as depicted in Fig. 7. In this process, blade deformations obtained by ANSYS Mechanical are mapped onto the corresponding mesh boundary in the fluidic domain in CFX. The deformations are mapped using a bucket search algorithm which preserves the profile of the deformation pattern. After the deformations are mapped on the

corresponding boundaries of the CFD mesh, the CFX deforms the rest of the CFD mesh using a displacement diffusion model with increased mesh stiffness near the blade boundaries in order to preserve the mesh quality in this region. On the other hand, loads in terms of exerted pressure on the blade's wetted surface obtained by CFX are mapped on the blade surface in ANSYS Mechanical. The mapping is performed using a tree search algorithm which ensures that the total transferred load is conserved. It is noteworthy that the mapping algorithms allow mapping onto a solid or a shell model on the structural side only. [19]

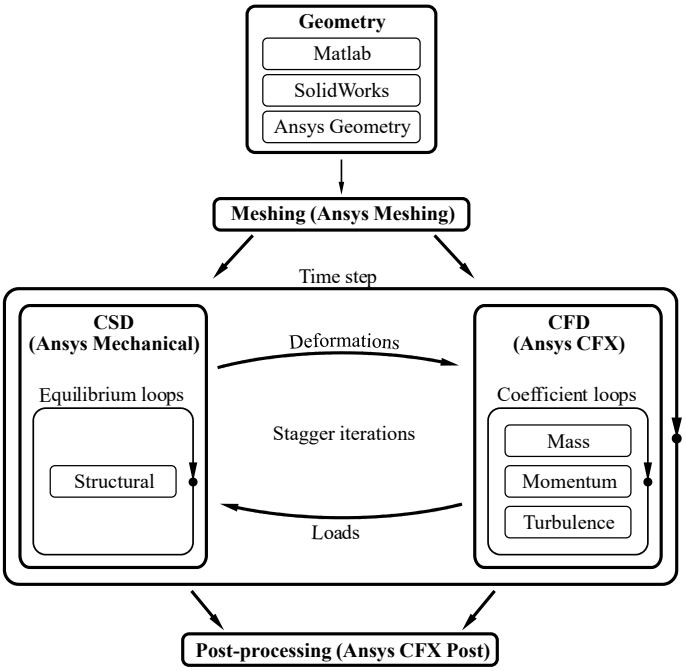

Figure 7. High-fidelity analysis outline

5 Results

The results of mesh convergence study are presented first in section 5.1. Validation results of the high-fidelity model are discussed in section 5.2. Outcome of the comparison between high- and low-fidelity model is presented in section 5.3.

5.1 Mesh Convergence Study

The procedure in which the mesh convergence study was performed is explained in section 4.1. The analysis was based on the SB blade. Since the BB and the FB blades are of the same size and studied under the same operating conditions, it is assumed that the same meshing parameters are appropriate for these two blades as well. Mesh convergence was established by monitoring the thrust coefficient, C_T, and the total mesh displacement near the tip of

the blade. Thrust coefficient and mesh displacement as a function of mesh size are depicted in Fig. 8. Both parameters converge in the same manner as the mesh is refined. Beyond the mesh size of $1 \cdot 10^7$ elements, the changes in C_T and total mesh displacement become very small. C_T changes by 0.1% and 0.2% and the total mesh displacement changes only by 0.002% and 0.005% as the mesh size is inflated from $1 \cdot 10^7$ elements to $2 \cdot 10^7$ and $7 \cdot 10^7$ elements, respectively. Therefore, the mesh of $1 \cdot 10^7$ elements was used in the high-fidelity simulations.

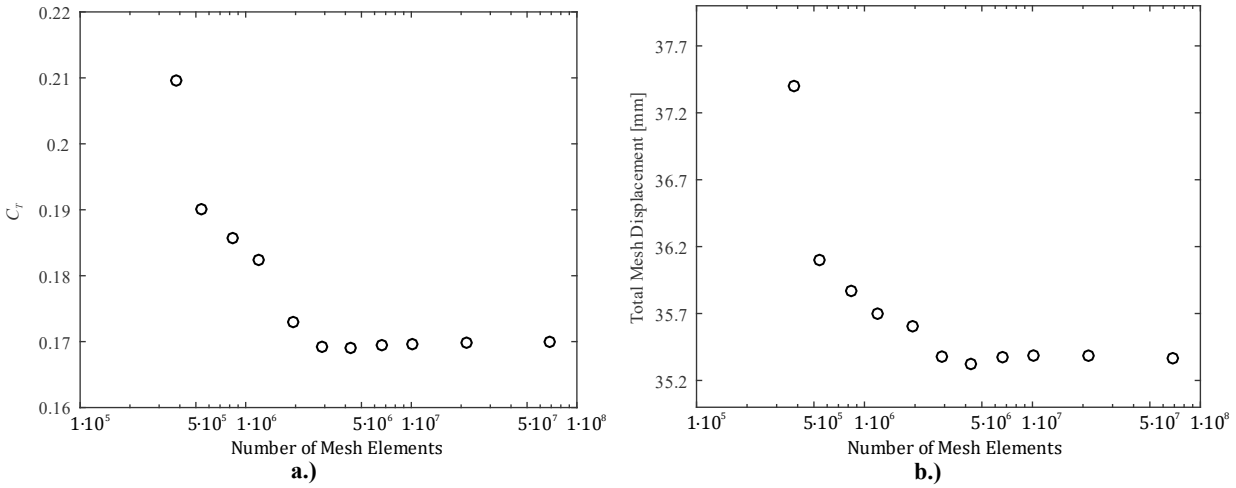

Figure 8. Mesh convergence measures: a.) thrust and b.) total mesh displacement

A representative pressure coefficient and total mesh displacement obtained on a BB blade at $J = 1.3$ are shown in Fig. 9.

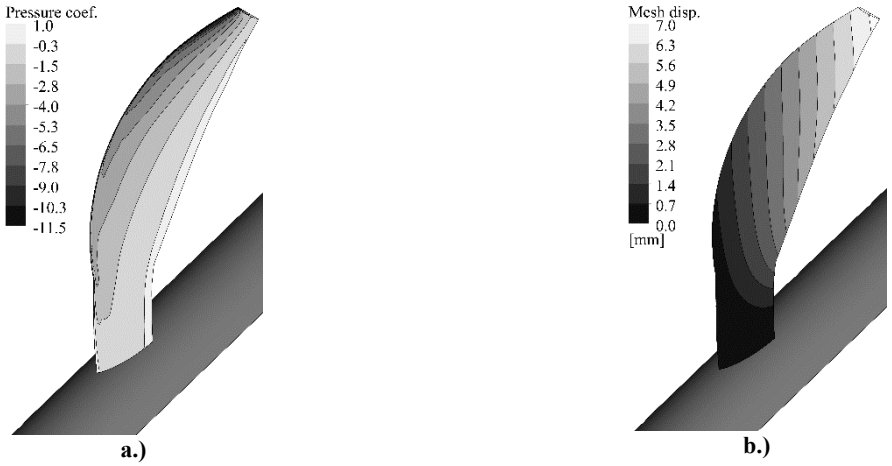

Figure 9: BB blade at $J = 1.30$: a.) pressure coefficient, and b.) total mesh displacement

5.2 Validation

Experimental results presented in [1] were used in order to validate the high-fidelity analysis. It is noteworthy that even though the advance ratios between the experiment and the design procedure are the same, the actual operating

conditions, namely the advance velocity and the propeller angular velocity, differ. One can observe that due to the aeroelastic coupling the actual operating conditions despite similar advance ratios affect the overall behavior of the blades. Hence, the high-fidelity simulations were adapted to run at actual experimental conditions for the purpose of validation. The rotor angular velocity was set at a constant $209\ \mathrm{rad/s}$, while the rotor advance velocity was varied from 13 up to $30\ \mathrm{m/s}$.

Integral aerodynamic characteristics C_T, C_P and η and out-of-plane tip deflection of the blade were reported in [1]. The comparison with the obtained numerical results is presented in Fig. 10. The C_T and the C_P coefficients are overpredicted by the high-fidelity simulations in general. However, in terms of qualitative relation between the different blades the high-fidelity results match the measurements very well. Both show similar trends and are in the same relative proportion for the different blade geometries. Relative to the BB and FB blade, considerably lower C_T and C_P are predicted for the SB blade by both measurements and the high-fidelity model. At $J = 1.30$, the ratios C_T^{SB}/C_T^{BB} and C_T^{SB}/C_T^{FB} evaluate to 0.76 and 0.74 for the measurements and to 0.82 and 0.77 for the high-fidelity results. Similarly, the C_P^{SB}/C_P^{BB} and C_P^{SB}/C_P^{FB} evaluate to 0.77 and 0.73 for the measurements, and to 0.80 and 0.75 for the high-fidelity results. The BB and FB blades show comparable C_T and C_P characteristics in both the measurements and the high-fidelity results. At $J = 1.30$, the ratio C_T^{FB}/C_T^{BB} evaluates to 0.99 for the measurements and to 1.07 for the high-fidelity results. The C_P ratio evaluates to 1.07 for both measurements and high-fidelity results. Furthermore, the drop in the efficiency of the SB blade at lower advance ratios relative to the BB and FB blade is observed by the measurements and predicted by the high-fidelity simulations. The only noticeable difference is at low advance ratios, where the high-fidelity C_T and C_P already plateaus, while the measurements continue to predict an increasing trend with decreasing J.

The high-fidelity structural response shown in Fig. 10d agrees with the experimental results very well both in qualitative as well as quantitative sense for the SB and the BB blade with an average difference of 6% and 8%, respectively. For the FB blade the agreement is worse with an average difference of 35%, which can be attributed to the differences observed in the aerodynamic loads obtained by the experiment and the high-fidelity FSI simulation.

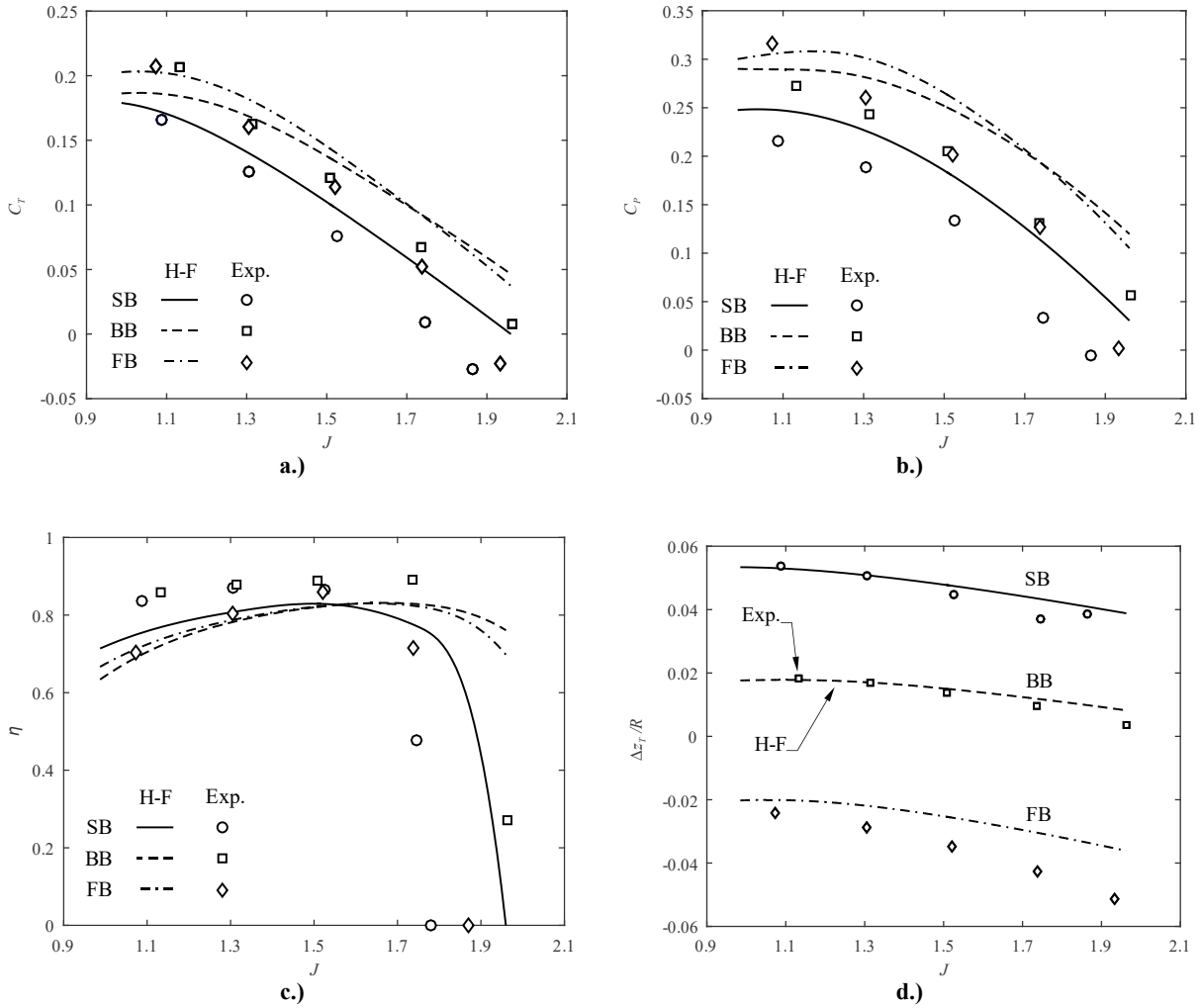

Figure 10. High-fidelity model validation: a.) C_T, b.) C_P, c.) η, and d.) blade tip out-of-plane deflection

5.3 Comparison of Low- and High-Fidelity Model

Low- and high-fidelity results for a range of advance ratios are discussed in the following section. First, the limitations stemming from the modelling assumptions for both high- and low-fidelity model are discussed in order to establish possible sources of differences observed in the results shown later on in this section. The discussion is followed by the comparison of the high- and low-fidelity structural models. The comparison is based on the response of the BB blade to a prescribed load. The aeroelastic results are discussed next. First the aerodynamic response in terms of thrust, power, and efficiency coefficients together with their respective distributions along the blade are compared followed by a comparison of the structural response. Structural response is compared in terms of blade elastic axis deflection and torsion.

Limitations of the low-fidelity model stem from the modelling assumptions in the structural and aerodynamic model. Structural model is based on geometrically exact Euler-Bernoulli theory for bending and Saint-Venant theory for torsion. Both models assume isotropic material with linear constitutive relations and sufficiently small strains to remain within the elastic range of deformation. The main assumption of the Euler-Bernoulli model is that the cross-section does not deform and remains perpendicular to the blade's elastic axis during deformation. Consequently, Euler-Bernoulli beam tends to appear stiffer in comparison to a full 3D FEM. Torsional response of the blades was described using the Saint-Venant theory which assumes that the cross-section does not deform in its own plane but it is allowed to warp out-of-plane. Furthermore, the Saint-Venant theory also assumes that the warping in all the cross-sections along the beam is the same and unrestrained. Hence, the effects of restrained warping at the blade root due to a clamped boundary condition are not accounted for which leads to more compliant blades in torsion [20].

The eBEM model of the low-fidelity model is a combination of the momentum theory and blade element theory. The momentum theory models the propeller as an infinitesimally thin actuation disk which imparts momentum on the fluid as it passes through such a disk. The imparted momentum is radially dependent on the local flow conditions of the corresponding blade element. The imparted momentum results in increased axial and circumferential velocity and is described by the axial and rotational interference factors, a_z and a_φ respectively, as previously shown in Fig. 4. The blade element theory is essentially a strip theory which considers each blade element as an independent 2D airfoil operating at some angle of attack, and Reynolds and Mach numbers. Thus, it is assumed that aerodynamic characteristics of each blade element is not affected by the adjacent elements. As a result, complex 3D flow phenomena such as radial flow, stall delay, and lift enhancement due to the rotation of the blade [21] and cross flow due to sweep of the blade [22] are not accounted for.

The deficiency of the eBEM model - not to account for the 3D flow effects, can be partially remedied by using experimental airfoil polars obtained on a rotating airfoil. However, such an extensive database was not available at the time of this study. Instead, Clark-Y airfoil C_L and C_D characteristics experimentally obtained by Lyon et al. [23] corresponding to the design operating conditions at 75% blade radius were used.

Finally, blade sweep was accounted for in the calculation of aerodynamic loads, dT/ds and dQ/ds by using the total velocity component in the plane of the airfoil normal to the blade axis, v^*, as can be seen in Eq. (2) and (3). In areas of large sweep, typically close to the tip of the blade, this can lead to a difference with respect to the high-fidelity CFD model.

Limitations of the high-fidelity model are more subtle. The main limitation of the full 3D non-linear FEM structural model is the assumption of linear material constitutive law over the entire range of experienced loads and deflections. In contrast to the low-fidelity structural model no assumptions regarding the cross-sectional deformations and warping are applied. However, the clamped boundary condition does restrain cross-sectional warping at the root of the blade, which stiffens the blades in the case of torsional loads.

The main modelling assumption of the CFD model is the usage of $k-\varepsilon$ turbulence model with scalable wall functions. $k-\varepsilon$ turbulence model belongs to the family of two-equation RANS models based on the eddy viscosity concept, which is based on the assumption of isotropic turbulence which is in equilibrium with the mean flow. In rotational flows however, due to rotational effects such as the Coriolis force, turbulence becomes anisotropic and is no longer in equilibrium with the mean flow which leads to increased turbulent kinetic energy generation and hence higher estimation of eddy viscosity [24]. It is however difficult, and beyond the scope of this paper to assess to what extent are the CFD results affected by violating the assumptions pertaining to the eddy viscosity hypothesis. However, as shown by Herráez et al. [25], two-equation RANS models with scalable wall functions have been successfully applied to investigation of rotating effects in the flows induced by wind turbine rotors.

5.3.1 Structural Model Comparison

High- and low-fidelity structural models are compared using the BB blade subjected to a tip force. The BB blade was selected due to its sweep, a curved elastic axis curved and a high degree of pre-twist which makes it a good representative of a general blade. Two orthogonal load cases, with the tip force oriented along $\vec{e}_y$ and $\vec{e}_z$, respectively, were selected for comparison. The selected load cases are depicted in Fig. 11.

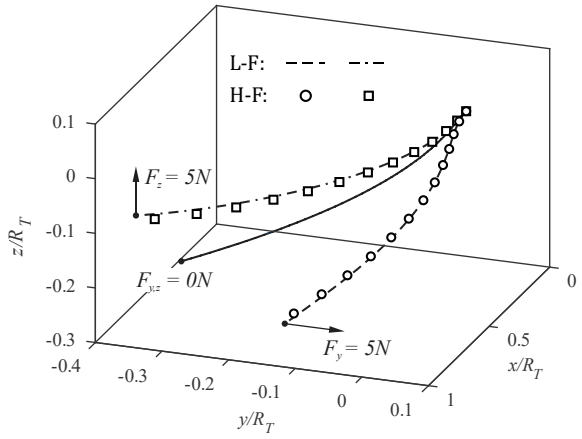

Figure 11: Applied load cases for structural model comparison

In each case the tip force was increased until the tip deflection reached the nonlinear range of about $0.15R_T$. The applied loads in combination with the selected blade geometry induce both bending and torsional deformation which allows for a comparison of both low-fidelity Euler-Bernoulli bending and Saint-Venant torsional model to the full 3D non-linear FEM model. The elastic axis deflections in y and z direction for each load case are shown in Fig. 12. The corresponding torsional deformations are shown in Fig. 13. The comparison of the two structural models in terms of relative tip deflections is summarized in Table 2.

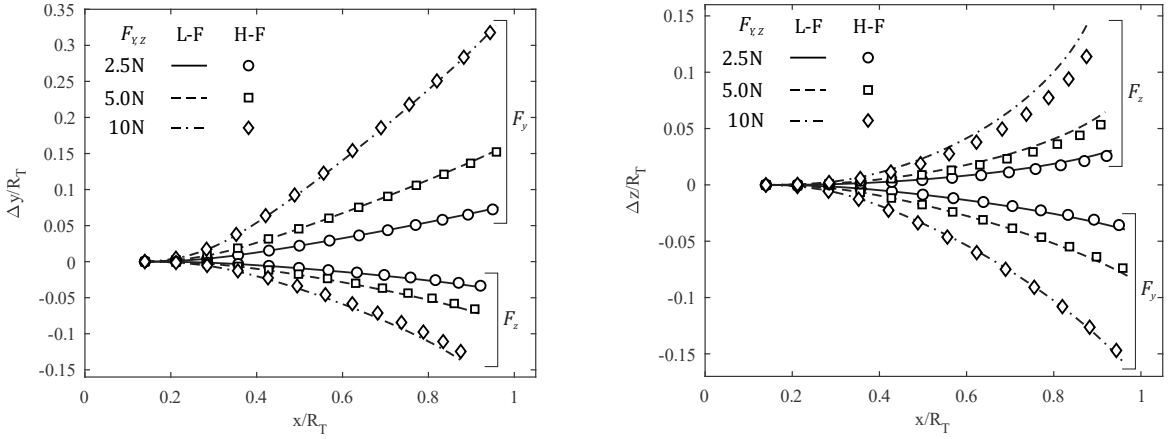

Figure 12: BB blade axis deflections due to tip force in $\vec{e}_y$ direction, a.) Δy vs. x and b.) Δz vs. x

The comparison of the out-of-plane deflections, Δy and Δz, in the case of F_y shows good agreement between low- and high-fidelity models with the difference being less than 1% and 7% in the respective direction regardless of the load magnitude. The difference between high- and low-fidelity model in the case of torsional deformation depends on the magnitude of the applied loads. It is increased from 4% up to 24% with increasing tip force which reflects the limitation of the low-fidelity Saint-Venant torsional model to small torsional deformations in the linear range.

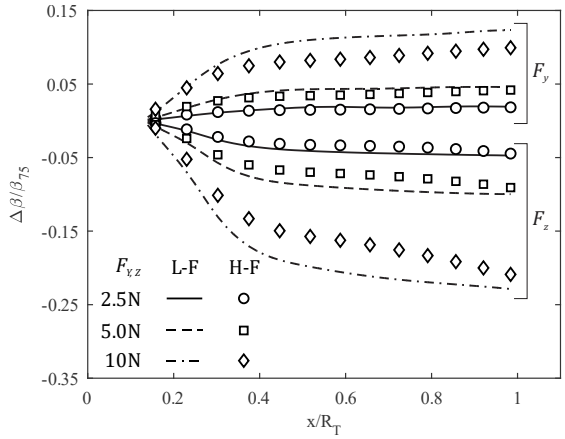

Figure 13: BB blade torsional deformation, $\Delta\beta$ vs. x, due to tip force in $\vec{e}_y$ direction

The comparison for the F_z load case yields larger differences between the low- and high-fidelity model. The difference in Δy and $\Delta\beta$ is constant at about 7% and 10% regardless of the load magnitude while the difference in Δz is increasing from 13% at the tip load of 5N load up to 20% at the tip load of 15N.

Table 2: Comparison of tip deflection under tip load

Load case	$\Delta y^{L-F}/\Delta y^{H-F}$	$\Delta z^{L-F}/\Delta z^{H-F}$	$\Delta\beta^{L-F}/\Delta\beta^{H-F}$
$F_y = 5N$	1.01	1.07	1.04
$F_y = 10N$	1.01	1.06	1.10
$F_y = 15N$	1.01	1.02	1.24
$F_z = 5N$	1.06	1.13	1.06
$F_z = 10N$	1.06	1.15	1.10
$F_z = 15N$	1.07	1.20	1.10

5.3.2 Aerodynamic Characteristics

A propeller blade is characterized by its integral thrust coefficient C_T, power coefficient C_P, and efficiency η at given advancing ratio J. The result comparisons for each coefficient are presented in Figs. 14, 15, and 16. Based on the results shown in Figs. 14a, 15a, and 16a one can conclude that the high- and low-fidelity methods agree very well in terms of trends. Both methods predict similar behavior of all three blades over the selected range of advance ratios. The predicted trends also agree, in a relative sense, when comparing the behavior of different blades to each other. At advance ratios below 1.3 the characteristics of the SB and BB blades is almost the same, however at advance ratios over 1.5 the BB outperforms the SB blade. Furthermore, both of the analysis methods predict almost the same value of J at which the SB and the BB blade transition to a wind milling mode.

Based on the normalized differences between the high- and low-fidelity results shown in Figs. 14b, 15b, and 16b three main observations can be highlighted. First, the best agreement between high- and low-fidelity results is achieved around the blade design advance ratio, $J = 1.30$. The difference between the high- and low-fidelity method is about 5% in C_T and η, and about 9% in C_P. Second, the low-fidelity method overpredicts C_T and η for advance ratios $J < 1.30$ with the difference increasing as the advance ratio is reduced. The difference can be attributed to the difference in stall modelling capabilities of the two fidelity models. Third, at advance ratios $J > 1.70$, the difference between the high- and low-fidelity models is rapidly increasing with the low-fidelity model strongly underpredicting the high-

fidelity model. The reason for such a behavior is that the blades are gradually transitioning into a wind milling regime which is marked by C_T and C_P approaching zero and by a sharp drop in efficiency. Consequently, small differences in C_T and C_P are amplified when normalized. In the case of η, the difference predominantly depends on the accuracy of the prediction of the wind milling transition point. Evidently, the low-fidelity model predicts the wind milling transition point at lower advance ratios relative to the high-fidelity model which is also reflected in the $\partial C_T/\partial\xi$ and $\partial C_P/\partial\xi$ lines at $J = 1.74$ and $J = 1.96$ shown in Figs. 17, 18, and 19. Early prediction of the wind milling transition point by the low-fidelity model is explained by considerably lower prediction of the wash-in along the SB blade, Fig. 24, and higher predictions of the wash-out along the BB and the FB blades shown in Figs. 25 and 26.

A reason for the differences in the results is also partially attributed to the fact that the dependence of the Clark Y aerodynamic properties on the Reynolds number were not accounted for in the low-fidelity analysis. The aerodynamic properties of the airfoil were chosen with respect to the estimated Reynolds number at 75% blade radius and applied over the entire blade span. However, the Reynolds number along the blade varies quite significantly from $50 \cdot 10^3$ at the root up to $400 \cdot 10^3$ at the tip of the blade. It can be observed in [23] that especially the drag of the Clark Y is strongly dependent on the Reynolds number. Still, the overall quantitative agreement between the low- and high-fidelity results is similar to the results reported by Kwon et al. [2] in their studies.

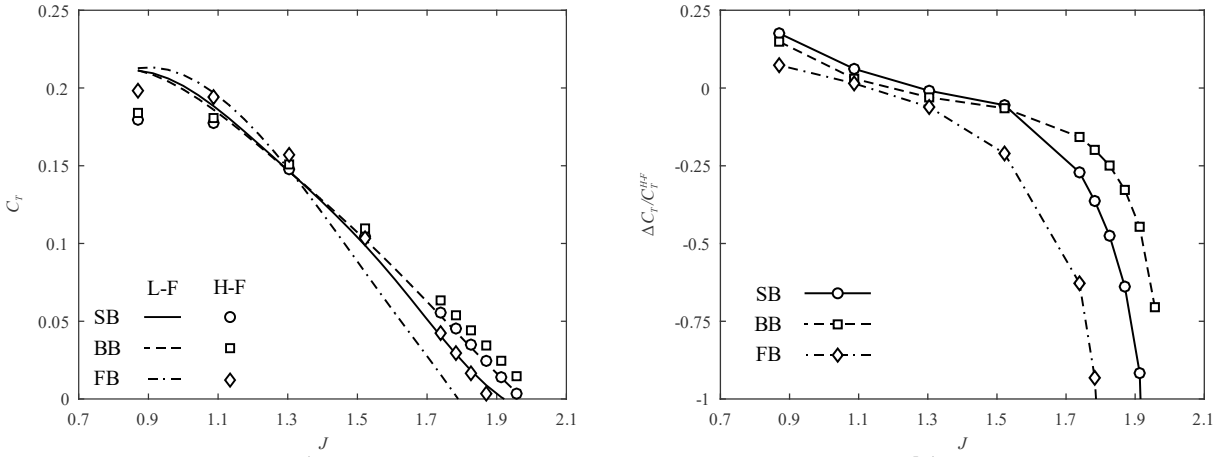

Figure 14. C_T as a function of J: a.) absolute values, and b.) normalized difference between high- and low-fidelity method

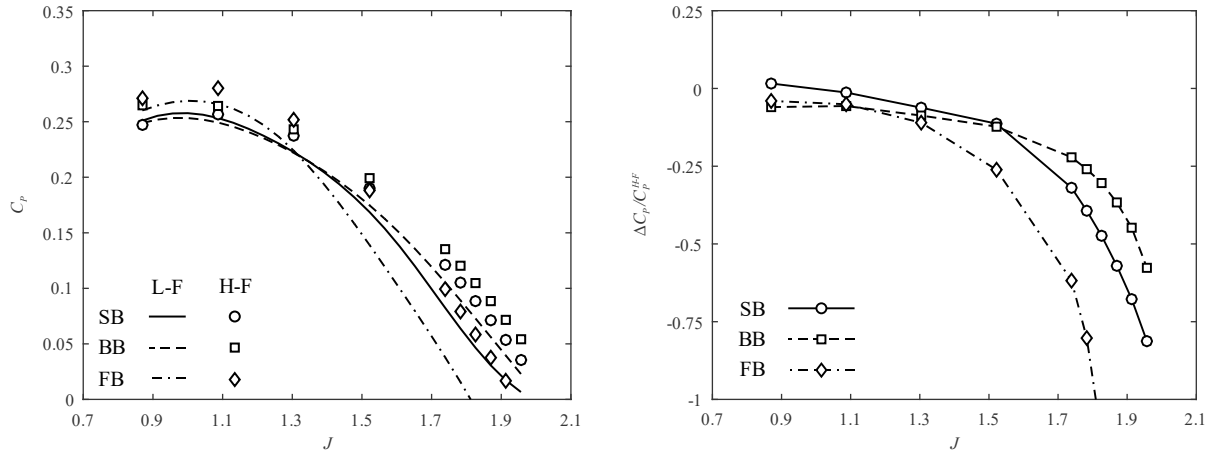

a.) b.)

Figure 15. C_P as a function of J: a.) absolute values, and b.) normalized difference between high- and low-fidelity method

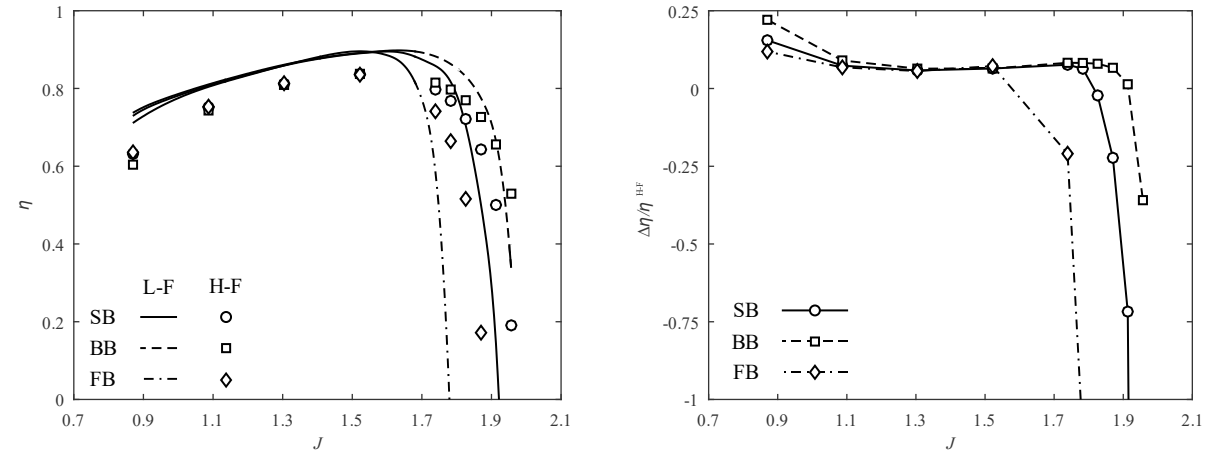

a.) b.)

Figure 16. η as a function of J: a.) absolute values, and b.) normalized difference between high- and low-fidelity method

Next, an analysis of the C_T and C_P distribution along the blade at different advance ratios was performed. Accuracy of the aerodynamic load distribution is important for an accurate prediction of the structural response and vice versa. The results for the SB, BB, and FB blades are shown in Figs. 17, 18, and 19, respectively. In general, the agreement between the high- and low-fidelity results is sufficient. Low-fidelity results generally underpredict the high-fidelity results in the case of the C_T distribution except for low advance ratios around $J = 0.89$. On the other hand, the difference among the selected result sets is larger in the case of the C_P distribution for all SB, BB, and FB blade geometries. In agreement with the integral C_P the low-fidelity C_P distributions underpredict the high-fidelity ones for all three blades.

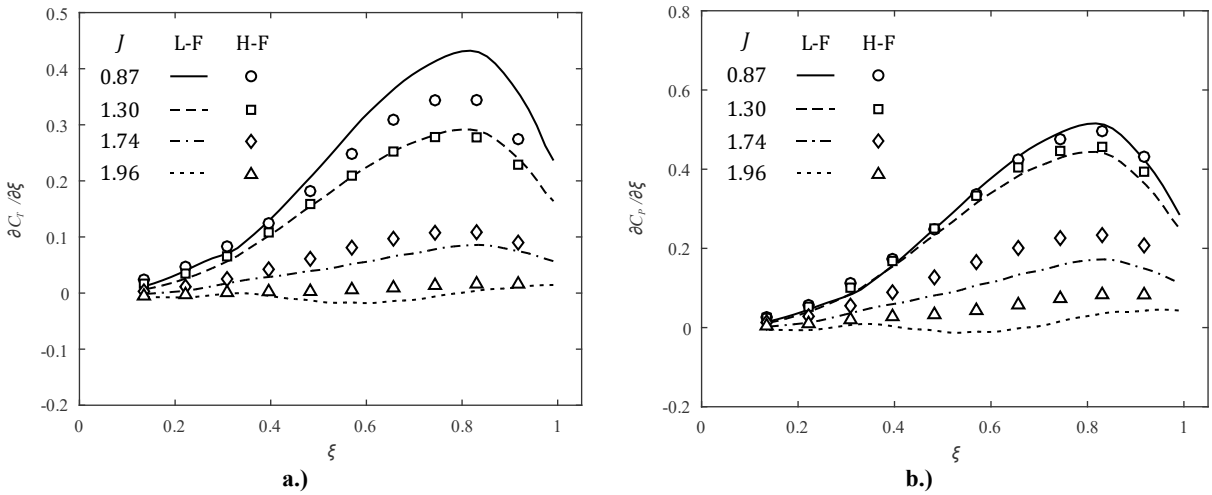

a.) b.)

Figure 17. C_T and C_P distribution along the SB blade, a.) and b.) respectively

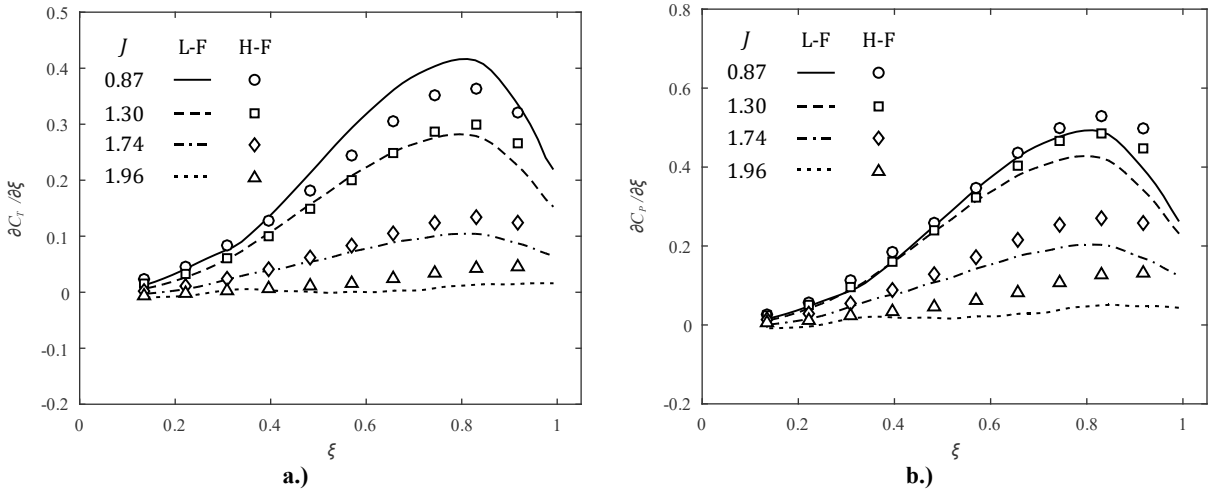

a.) b.)

Figure 18. C_T and C_P distribution along the BB blade, a.) and b.) respectively

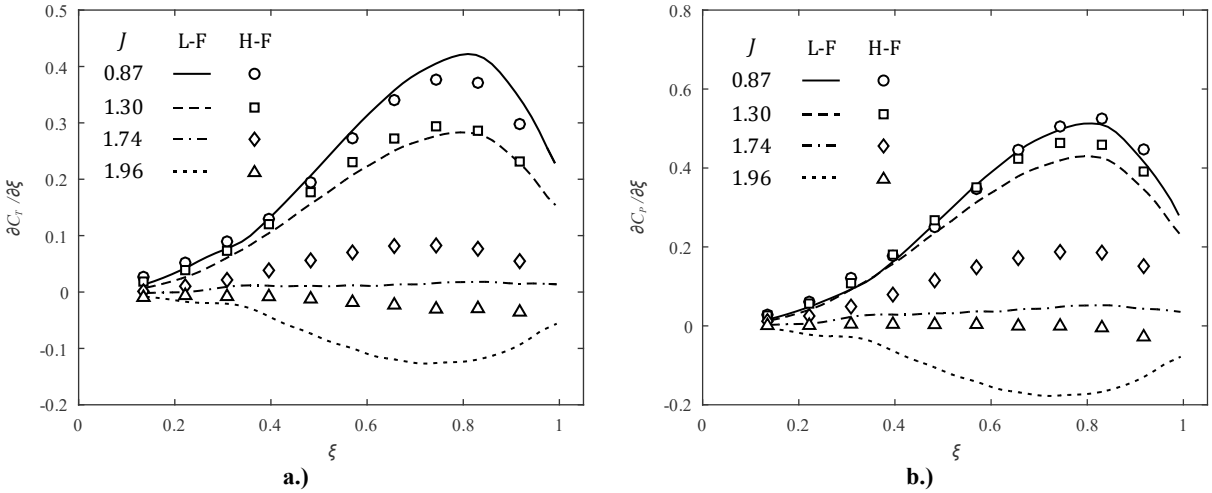

a.) b.)

Figure 19. C_T and C_P distribution along the FB blade, a.) and b.) respectively

5.3.3 Structural Aeroelastic Response

Structural aeroelastic response of the blades is analysed by comparing the predicted deflections of the blade axis in y and z coordinate direction and twist around the blade elastic axis. The deflection results for each blade type are presented in Figs. 20, 21, and 22. The twist results for each individual blade are shown in Figs. 24, 25, and 26.

In the case of Δy and Δz deflections, agreement among the high- and low-fidelity results depends on the blade type as can be observed in Tables 3 and 4 comparing the tip deflections at various advance ratios. In the case of the SB blade excellent agreement is observed with differences no larger than 6%. The worst agreement is observed in the case of the BB blade, with differences up to 70%. However, the overall deflections in the case of BB blade are quite small, about $0.03R_T$.

Consistent response with respect to the companion aerodynamic part of the simulations is observed. In the cases where the low-fidelity model underpredicts the loading along the blade, the deflections of the corresponding blades are underpredicted as well. However, it is important to define the underpredicted results correctly with respect to the nature of the interaction among inertial and aerodynamic forces. For instance, in the case of the BB blade, the Δz deflections predicted by the low-fidelity analysis are greater than those determined by the high-fidelity method, even though the aerodynamic forces predicted by the low-fidelity analysis are smaller than those predicted by the high-fidelity one. In this case the aerodynamic and inertial forces oppose each other. Consequently, the smaller the aerodynamic load the bigger the deflection due to the opposing inertial force.

Table 3: Tip deflection comparison: Δy

	$\Delta y^{L-F}/\Delta y^{H-F}$			
$J=$	0.89	1.30	1.74	1.96
SB	1.06	1.01	0.97	0.97
BB	1.71	1.41	1.02	1.06
FB	0.84	1.09	1.20	1.20

Table 4: Tip deflection comparison: Δz

	$\Delta z^{L-F}/\Delta z^{H-F}$			
$J=$	0.89	1.30	1.74	1.96
SB	1.06	1.01	0.97	0.97
BB	1.45	1.33	1.34	1.38
FB	0.93	1.01	1.09	1.08

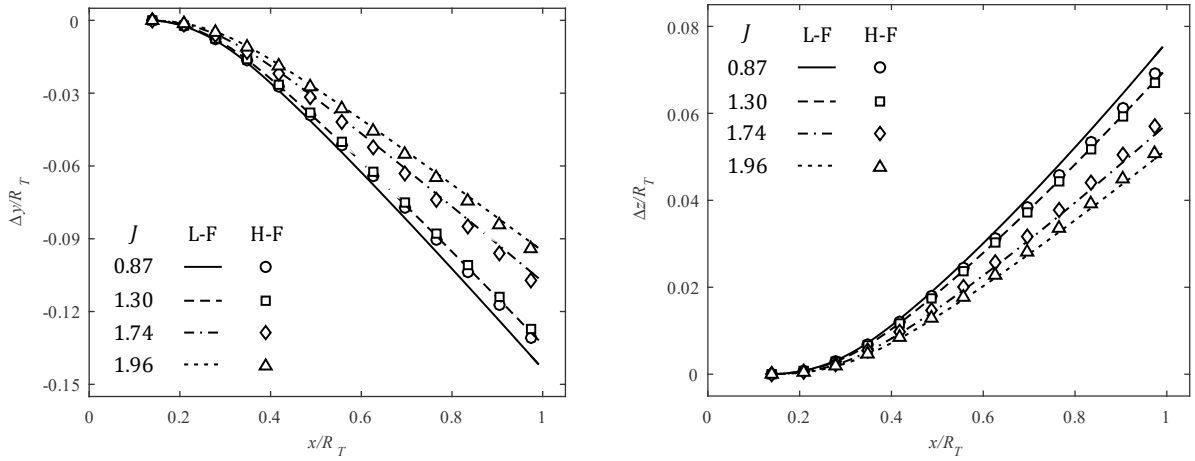

a.) b.)

Figure 20. SB blade axis deflections at different advance ratios, a.) Δy vs. x and b.) Δz vs . x

One can observe in Fig. 21a that the root part of the blade deflects in the opposite direction than the tip at $J = 1.74$ and $J = 1.96$. Such behavior is captured by both low- and high-fidelity analysis. It is also noticeable that at $J = 0.87$, the mismatch between the high- and low-fidelity analysis is considerably higher than in the other cases, which is attributed to a more complex interaction between the aerodynamic, inertial, and structural loads. Therefore, it can be concluded that the low-fidelity model can capture such a complex behavior, however it should be used with caution as the blades become exceedingly swept.

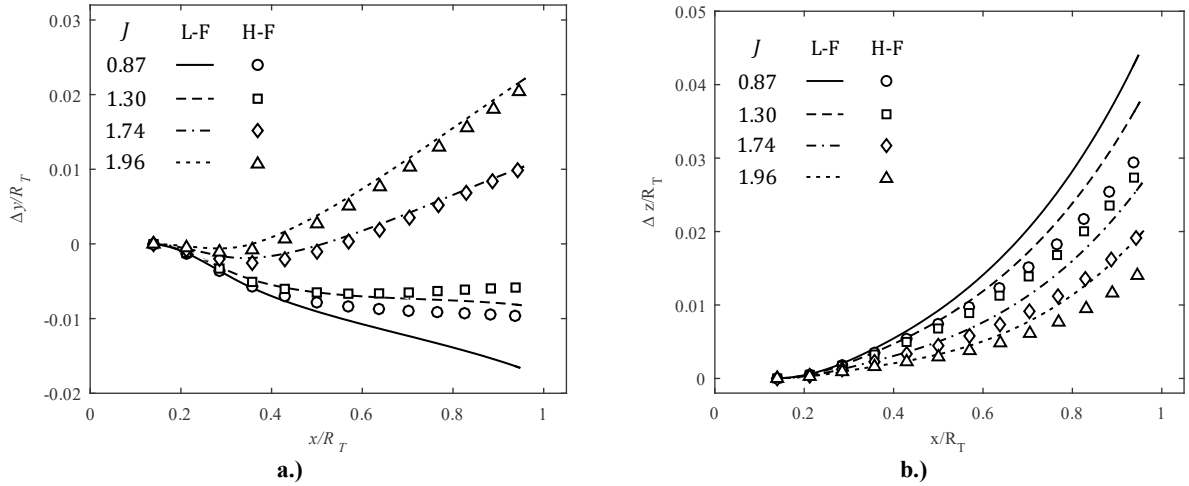

a.) b.)

Figure 21. BB blade axis deflections at different advance ratios, a.) Δy vs. x and b.) Δz vs. x

The comparison between low- and high-fidelity results in the case of the FB blade yields similar observations as in the case of the BB blade. These results are presented in Fig. 22. The match of the Δz displacements over the entire

length of the blade and the entire range of the advance ratios is good with differences being less than 9%. The agreement in y direction is somewhat worse with differences up to 20%.

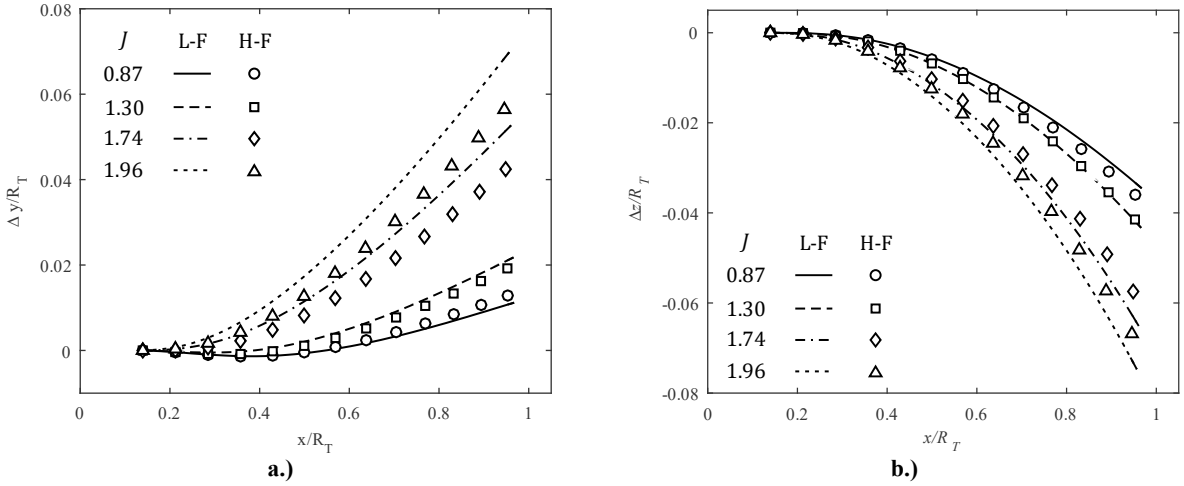

Figure 22. FB blade axis deflections at different advance ratios, a.) Δy vs. x and b.) Δz vs. x

The twist induced by the applied loads is discussed next. Torsional deformation is strongly coupled to the blade's undeformed shape. The most important geometrical parameters are the sweep and the coning of the blade. The sweep provides leverage to aerodynamic loads while coning provides leverage to the centrifugal inertial loads. Depending on the sweep direction, the aerodynamic loads can either cause blade to wash-in or wash-out. Inertial loads always bend the blade towards the plane of rotation passing through the rotor hub. The effect of coning is shown in Fig. 23. The influence of the centrifugal force is especially important for the swept forward blades, since it prevents blades from diverging. Such behavior is clearly observed in the torsional response of the SB and FB blade shown in Figs. 24 and 26 respectively. Both blades are swept forward in their undeformed configuration hence their response is to wash in as the aerodynamic loads are increased. However, the SB blade has negative coning (in the direction of the flow), hence, the aerodynamic and inertial loads act in the same direction and the SB blade is actually diverging for small advance ratios. As the aerodynamic loads decrease the SB blade's torsional deformation becomes more or less negligible. On the other hand, the FB blade has positive coning. Consequently, the aerodynamic and inertial loads act in the opposite direction. Hence the blade exhibits wash out already at low advance ratios, however, as the advance ratio is increased the aerodynamic loads decrease and the inertial loads can further increase the wash out of the blade. On the other hand, the BB blade has a negative coning as well as sweep backward. Hence, both aerodynamic and inertial loads tend to wash out the blade, which can be observed in the Fig. 25. Moreover, one can observe that with

increasing the advance ratio, the amount of wash out is indeed decreased, since the aerodynamic loads decrease. In this regard, qualitatively, the low- and high-fidelity results agree well.

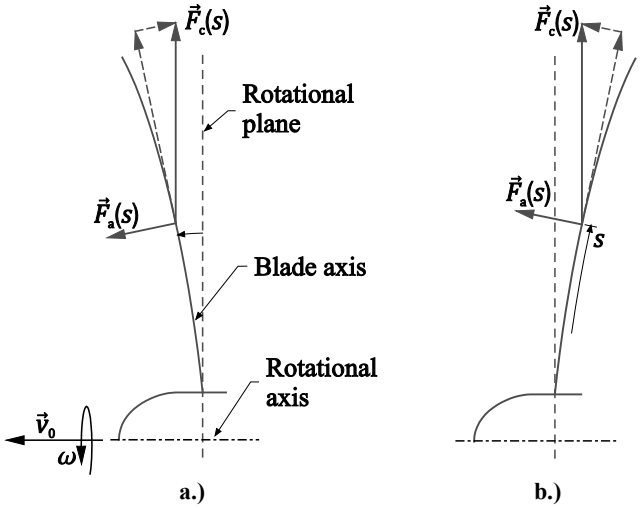

Figure 23: Leverage to centrifugal loads due to a.) positive coning, and b.) negative coning

Tip twist of the blades is compared in Table 5 in order to quantify the agreement between high- and low-fidelity results. By far the worst agreement is observed in the case of the SB blade. However, the amount of torsional deformation present in the SB blade is also very low, at maximum $0.04\beta_{75}$ and $0.02\beta_{75}$ for the high- and low-fidelity model respectively. The differences for the BB and the FB blade are consistent with those observed in the tip deflection results, around 20% and 10%, respectively.

Finally, in terms of comparison, the computational costs required to perform these simulations are addressed. Both high- and low-fidelity results were obtained using an Intel(R) Xeon(R) CPU E5-2640 v4 processor. High-fidelity simulations were run in parallel using 20 processing cores while the low-fidelity simulations were run in Matlab using a single processing core. On average, the high-fidelity simulations required 140 hours of processing time per simulation case per blade. In contrast the low-fidelity simulations required 430s of processing time for the same job which equals to ~0.1% of the time used by the high-fidelity simulation.

Table 5: Tip twist comparison: $\Delta\beta$

	$\Delta\beta^{L-F}/\Delta\beta^{H-F}$			
$J=$	0.89	1.30	1.74	1.96
SB	0.54	0.33	-0.36	0.18
BB	1.25	1.26	121	1.19
FB	1.01	1.09	1.18	1.07

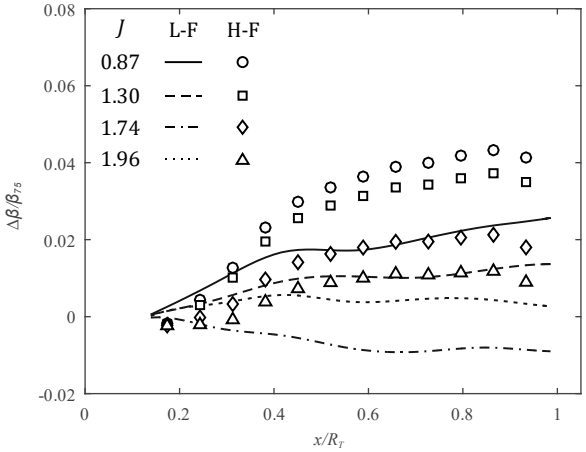

Figure 24: SB blade twist at different advance ratios

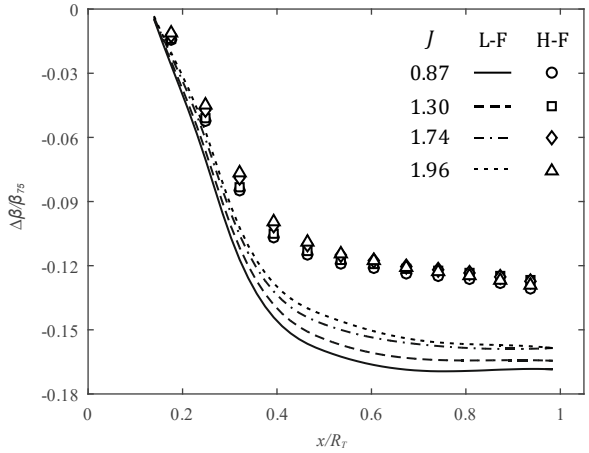

Figure 25: BB blade twist at different advance ratios

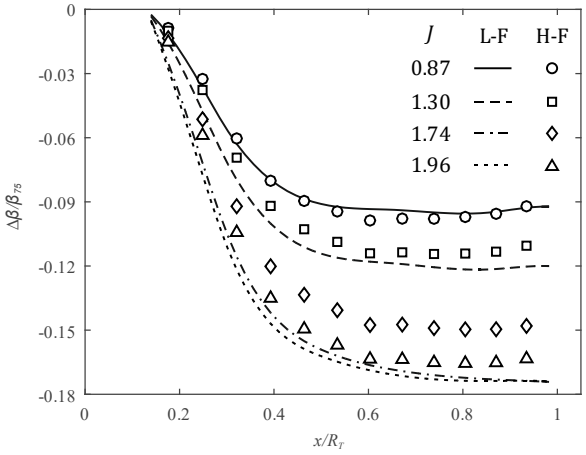

Figure 26: FB blade twist at different advance ratios

5.4 Advance ratio in the case of flexible propeller blades

It was noticed in section 5.2 that the performance of the FB blade relative to the SB and the BB blade was not in agreement with the initial design expectations for this blade. The FB blade was expected to perform the worst over

the range of selected advance ratios since the blades were tested at the same advance ratios used in the design process. The operating conditions in terms of free stream and propeller rotational velocity were however different. To gain a better insight into how the actual operating conditions affect the performance of a flexible blade, an aeroelastic analysis of all three blades at various operating conditions corresponding to a constant advance ratio is performed in this section.

In the current study, the advance ratio was set to 1.30 which corresponds to the blade design advance ratio and the propeller rotational speed, n, was varied in the range from $1500\ rpm$ up to $4500\ rpm$ around the design rotational speed, n_{DP}, of $3000\ rpm$. Aerodynamic performance of the blades in terms of C_T, C_P, and η is shown in Fig. 27. Both low- and high-fidelity results are presented. Coefficient variation, ΔC_T, ΔC_P, and $\Delta\eta$, over the range of investigated rotational speeds are summarized in Table 6. The coefficient variations are defined as a difference between the maximum and minimum coefficient value normalized with the coefficient value at n_{DP}: $\Delta C_T = \left(C_T^{max} - C_T^{min}\right)/C_T^{DP}$, $\Delta C_P = \left(C_P^{max} - C_P^{min}\right)/C_P^{DP}$, and $\Delta\eta = (\eta^{max} - \eta^{min})/\eta^{DP}$.

A significant difference is observed in the behavior between the SB and the BB and FB blades. In the case of the SB blade both C_T and C_P linearly increase with increasing rotational velocity, whereas they nonlinearly decrease in the case of the BB and FB blade. Moreover, the variation in thrust and power coefficients over the range of investigated rotational speeds is considerably larger in the case of the two swept blades. According to the low-fidelity model $\Delta C_T = 6\%$ for the SB blade while $\Delta C_T = 77\%$ for the BB blade and $\Delta C_T = 96\%$ for the FB blade. Similarly, for the SB blade $\Delta C_P = 6\%$, while for the BB and FB blade $\Delta C_P = 84\%$ and 101% respectively.

There is less difference among the three blades in the case of efficiency, η. $\Delta\eta$ is relatively small for all three blades despite large ΔC_T and ΔC_P in the case of the BB and FB blade. Efficiency of the SB blade shows the least variation and is almost constant over the entire range of investigated rotational velocities with $\Delta\eta = 0.6\%$ and $\Delta\eta = 0.2\%$ according to low- and high-fidelity model respectively. The efficiency of the BB and FB blade varies up to 7% and 4% respectively according to the low-fidelity model and 8% and 7% according to the high-fidelity model.

Large variations in ΔC_T and ΔC_P observed in Fig. 27 can be explained by investigating the aeroelastic deformation of the selected blades over the range of selected rotational speeds. Blade tip deflection, Δy_T and Δz_T, and tip twist, $\Delta\beta_T$ are shown in Fig. 28. Evidently, as rotational speed is increased large deformations are induced. SB blade exhibits large variation in Δy_T and Δz_T and small variation in $\Delta\beta_T$ in comparison to the BB and FB blade.

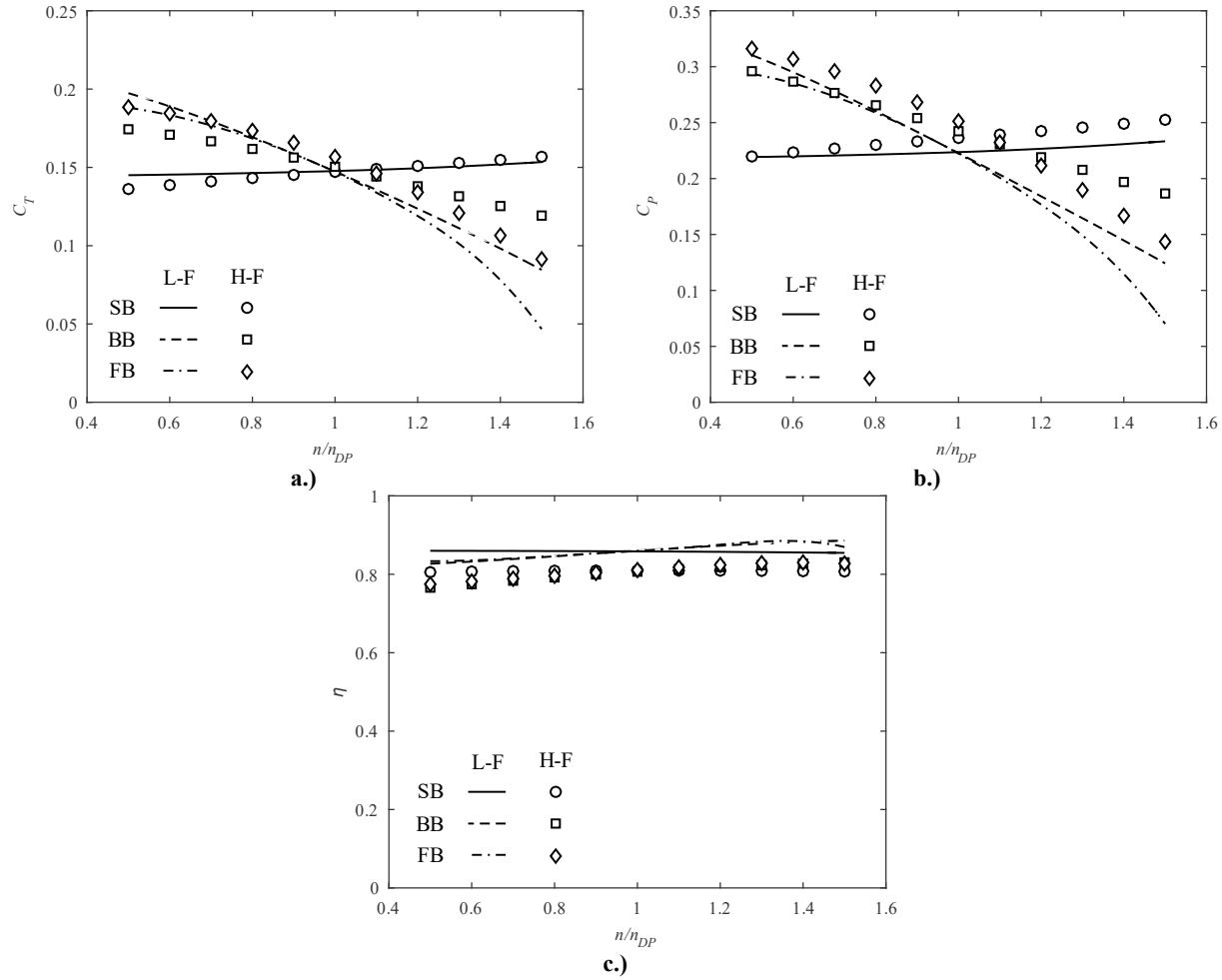

Figure 27: Performance characteristics of the SB, BB, and FB blade as a function of propeller rotational velocity at $J = 1.30$: a.) thrust coefficient C_T, b.) power coefficient C_P, and c.) efficiency η

Based on the shown deformations one can conclude that low susceptibility of the SB blade to the changing rotational velocity is attributed to the lack of sweep. First, lack of sweep results in a smaller torsional moment due to acting aerodynamic and inertial loads which in turn leads to comparatively smaller $\Delta\beta$ along the blade. Second, lack of sweep results in a lack of geometric bend-twist coupling typical for swept wings [26]. Hence, even though SB blade exhibits large Δy_T and Δz_T, these deformations marginally affect the overall 'aerodynamic' twist of the blade. In the case of the BB and FB blade, the 'aerodynamic' twist is also affected by the bending deformations Δy and Δz. Consequently, BB and FB blade performance depends more on the actual operating conditions such as the rotational speed of the propeller.

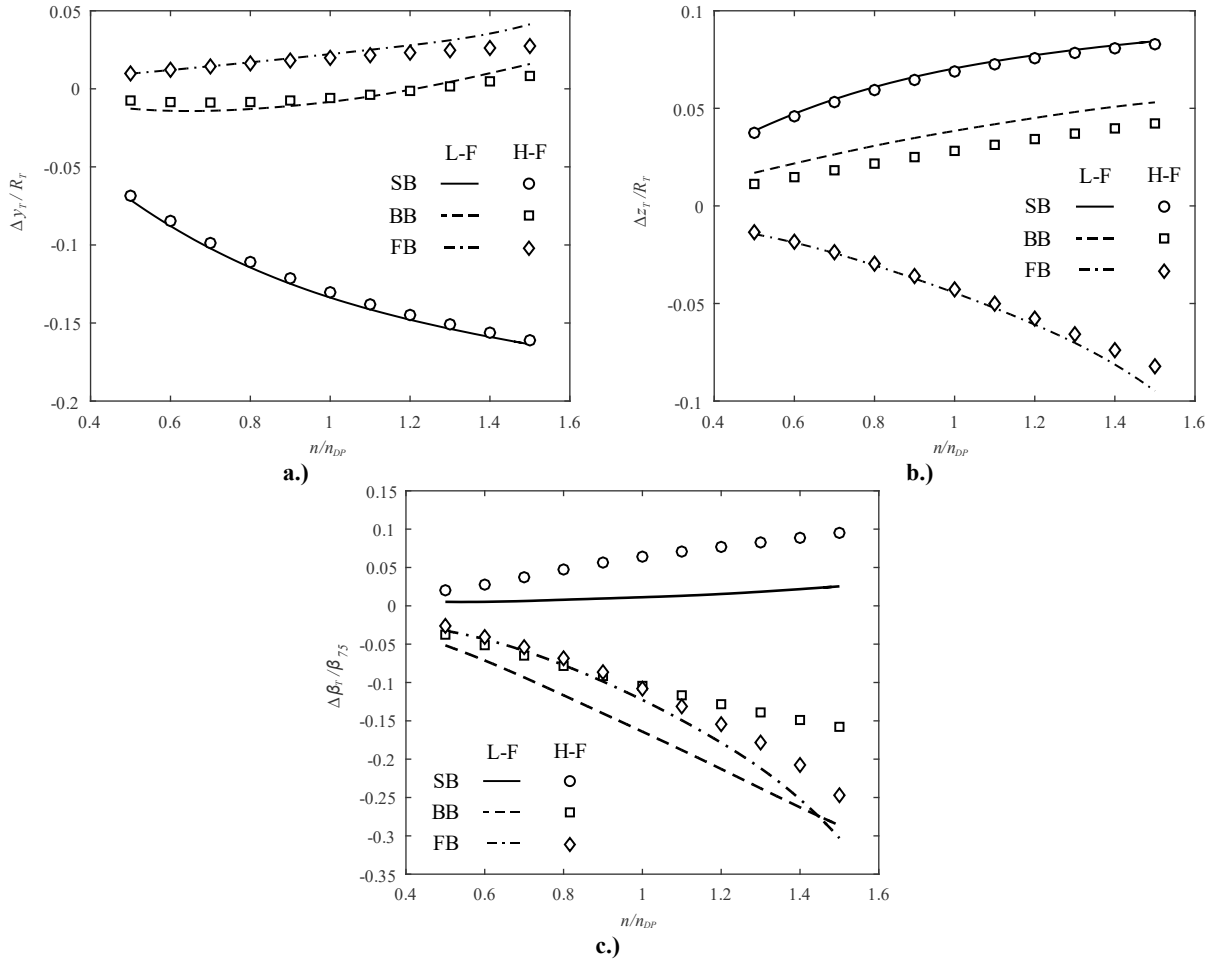

Figure 28: Tip deformation of the SB, BB, and FB blade as a function of propeller rotational velocity at $J = 1.30$: a.) in-plane, b.) out-of-plane and c.) twist deformation

Table 6: Summary of C_T, C_P, and η variation at $J = 1.30$

	SB		BB		FB	
	L-F	H-F	L-F	H-F	L-F	H-F
ΔC_T	0.057	0.140	0.766	0.366	0.961	0.619
ΔC_P	0.063	0.138	0.836	0.451	1.006	0.687
$\Delta\eta$	0.006	0.002	0.068	0.080	0.041	0.065

Low- and high-fidelity results are consistent in terms of observed trends for all three blade types and for all performance coefficients and deformations shown in Figs. 27 and 28. However, one can observe the low-fidelity results tend to diverge from the high-fidelity results beyond the design rotational speed, n_{DP}. As a result, large differences of 45% up to 110% are observed in the calculated coefficient variations, ΔC_T, and ΔC_P as shown in Table 6. However, the differences between the high- and low-fidelity results are consistent across the C_T and C_P which

results in a good absolute agreement between the two models in the case of Δη. Similar order of difference between high- and low-fidelity model is also observed in deformation results shown in Fig. 28.

6 Conclusions

A verification of the low-fidelity flexible propeller blade model based on the extended blade element momentum aerodynamic model and the non-linear geometrically exact Euler-Bernoulli beam structural model is carried out by comparing the results with a high-fidelity two-way FSI model implemented in ANSYS CFX and ANSYS Mechanical. Sufficient quality of the high-fidelity results was ensured by performing mesh convergence study. Convergence studies served as a reference for setting up the high-fidelity FSI simulations. The high-fidelity model was also validated against experimental findings.

A detailed comparison of the low- and high-fidelity method was facilitated by analysing three distinct blade geometries at various advance ratios. A comparison of the aerodynamic properties like thrust, breaking power and efficiency with their respective distributions along the blade span was performed. In terms of structural analysis, blade deflections along y and z coordinate directions and blade twist along the blade axis were studied.

A good agreement between the low- and the high-fidelity results was observed. The low-fidelity results generally underpredict the aerodynamic loads on the blades. Consequently, some difference in the prediction of structural deflections is also observed. These differences are, however, in agreement with the differences observed in the aerodynamic loads.

In order to improve the accuracy of the low-fidelity model improvements of the extended blade element momentum model were suggested. For instance, addition of the Reynolds number effect on the airfoil properties and improved treatment of the blade sweep necessary for moderately and highly swept blades.

Overall, the low-fidelity model was proved to be very effective at predicting the general behavior of the investigated blades, none of the important features in terms of qualitative behavior are missed. The low-fidelity model successfully captured aeroelastic coupling effects such as increased efficiency of the backward swept blade with respect to the forward-swept and the straight blade at higher advance ratios, wash-in of the straight blade and wash-out in the case of the backward swept and the forward swept blade.

Advance ratio is one of the most common non-dimensional parameters used to ease and generalize the comparison between propellers of various shape and size which are often operated or tested at different operating conditions. It

was shown that advance ratio as a measure of similarity breaks down in the case of flexible propeller blades if the rotational speed of the propeller is changed which prevents generalization of such results. This has strong implications, for instance, when the results are used in the scale-up study which is often the case with the experimental results or if the same propeller characteristics are used at varying operating conditions in a design study. Therefore, in the case of flexible propeller blades, care must be taken when generalizing non-dimensional trends obtained at certain specific operating conditions.

7 References

[1] J. Sodja, R. Drazumeric, T. Kosel, and P. Marzocca, 'Design of Flexible Propellers with Optimized Load-Distribution Characteristics', *J. Aircr.*, vol. 51, no. 1, pp. 117–128, 2014.

[2] H.-I. Kwon, S. Yi, S. Choi, and K. Kim, 'Design of Efficient Propellers Using Variable-Fidelity Aerodynamic Analysis and Multilevel Optimization', *J. Propuls. Power*, vol. 31, no. 4, pp. 1057–1072, Jul. 2015.

[3] L. Piancastelli, A. Castagnoli, L. Frizziero, G. Donnici, and S. Pica, 'Direct comparison of fsi optimized theodorsen and larrabee propellers', *ARPN J. Eng. Appl. Sci.*, vol. 10, no. 16, pp. 7250–7258, 2015.

[4] N. Nigam *et al.*, 'Multi-Fidelity Multi-Disciplinary Propeller/Rotor Analysis and Design', 2015.

[5] B. M. Tojo and A. C. Marta, 'Aero-Structural Blade Design of a High-Power Wind Turbine', in *54th AIAA/ASME/ASCE/AHS/ASC Structures, Structural Dynamics, and Materials Conference*, American Institute of Aeronautics and Astronautics.

[6] Y. Bazilevs, M.-C. Hsu, J. Kiendl, R. Wüchner, and K.-U. Bletzinger, '3D simulation of wind turbine rotors at full scale. Part II: Fluid–structure interaction modeling with composite blades', *Int. J. Numer. Methods Fluids*, vol. 65, no. 1–3, pp. 236–253, Jan. 2011.

[7] Y. Bazilevs, M.-C. Hsu, J. Kiendl, and D. J. Benson, 'A computational procedure for prebending of wind turbine blades', *Int. J. Numer. Methods Eng.*, vol. 89, no. 3, pp. 323–336, 2012.

[8] M. E. Braaten, C. Seeley, and M. Tooley, 'High Fidelity Fluid-Structure Interaction Analysis of a Wind Turbine Blade', in *54th AIAA/ASME/ASCE/AHS/ASC Structures, Structural Dynamics, and Materials Conference*, American Institute of Aeronautics and Astronautics.

[9] M.-C. Hsu and Y. Bazilevs, 'Fluid-structure interaction modeling of wind turbines: Simulating the full machine', *Comput. Mech.*, vol. 50, no. 6, pp. 821–833, 2012.

[10] C. N. Adkins and R. H. Liebeck, ‘Design of optimum propellers’, *J. Propuls. Power*, vol. 10, no. 5, pp. 676–682, 1994.

[11] ANSYS, ‘15. Advice on Flow Modeling // 15.3. Mesh Issues // 15.3.2. Measures of Mesh Quality’, in *ANSYS CFX Modeling Guide*, Canonsburg, PA: ANSYS, Inc., 2013.

[12] P. Catalano and M. Amato, ‘An evaluation of RANS turbulence modelling for aerodynamic applications’, *Aerosp. Sci. Technol.*, vol. 7, no. 7, pp. 493–509, 2003.

[13] S. Brizzolara, D. Villa, and S. Gaggero, ‘A systematic comparison between RANS and panel methods for propeller analysis’, in *Hydrodynamics VIII, 8th International Conference on Hydrodynamics, ICHD 2008*, 2008.

[14] L. Veldhuis and G. Luursema, ‘Comparison of an actuator disk and a blade modeling approach in Navier-Stokes calculations on the SR-3 propfan’, in *18th Applied Aerodynamics Conference*, American Institute of Aeronautics and Astronautics.

[15] J. Sodja, D. Stadler, and T. Kosel, ‘Computational fluid dynamics analysis of an optimized load-distribution propeller’, *J. Aircr.*, vol. 49, no. 3, pp. 955–961, 2012.

[16] S. Bechet, C. Negulescu, V. Chapin, and F. Simon, ‘Integration of CFD tools in aerodynamic design of contra-rotating propellers blades’, 2011.

[17] B. G. Marinus, ‘Comparative Study of Effects of Sweep and Humps on High-Speed Propeller Blades’, *AIAA J.*, vol. 52, no. 4, pp. 739–746, 2014.

[18] ANSYS, ‘I. Element Library // SOLID186’, in *Mechanical APDL Modeling Guide*, Canonsburg, PA: ANSYS, Inc., 2013.

[19] ANSYS, ‘4. Multi-field Analysis Using Code Coupling’, in *Coupled-Field Analysis Guide*, Canonsburg, PA: ANSYS, Inc., 2017.

[20] S. Timoshenko and J. N. Goodier, *Theory of elasticity*, 3rd ed. New York: McGraw-Hill, 1987.

[21] H. Himmelskamp and Aerodynamische Versuchsanstalt Göttingen, *Profile investigations on a rotating airscrew*. Geottingen, Germany: MAP Völenrode, 1947.

[22] R. Vos and S. Farokhi, *Introduction to Transonic Aerodynamics*, vol. 110. Dordrecht: Springer Netherlands, 2015.

[23] C. A. Lyon, A. P. Broeren, P. Giguere, A. Gopalarathnam, and M. S. Selig, *Summary of Low-Speed Airfoil Data*, vol. 3. Virginia Beach, Virginia, USA: SoarTech Publications.

[24] H.-H. Tsuei and J. Perot, 'Advanced turbulence model for transitional and rotational flows in turbomachinery', 2000.

[25] I. Herráez, B. Stoevesandt, and J. Peinke, 'Insight into Rotational Effects on a Wind Turbine Blade UsingNavier–Stokes Computations', *Energies*, vol. 7, no. 10, pp. 6798–6822, Oct. 2014.

[26] D. H. Hodges and G. A. Pierce, *Introduction to structural dynamics and aeroelasticity*, 2nd ed. New York: Cambridge University Press, 2011.